Charged-particles measurements in low-pressure iodine plasmas used for electric propulsion

B Esteves, F Marmuse, C Drag, A Bourdon, A Alvarez Laguna, P Chabert

Plasma Sources Science and Technology

Charged-particles measurements in low-pressure iodine plasmas used for electric propulsion

To cite this article before publication: Benjamin Esteves *et al* 2022 *Plasma Sources Sci. Technol.* in press https://doi.org/10.1088/1361-6595/ac8288

Charged-particles measurements in low-pressure iodine plasmas used for electric propulsion

B. Esteves[1], F. Marmuse[1], C. Drag[1], A. Bourdon[1], A. Alvarez Laguna[1], P. Chabert[1]

[1]Laboratoire de physique des plasmas, Centre National de la Recherche Scientifique, Ecole polytechnique, Institut polytechnique de Paris, Palaiseau, Île-de-France, 91128, FRANCE

June 2022

Abstract. This paper investigates iodine as an alternative propellant for space plasma propulsion. Measurements are taken in a low-pressure inductively-coupled plasma chamber used as the ionisation stage of a gridded ion-engine. Langmuir probes are used to measure the electron density and the electron energy distribution functions spatial variations between the inductive coil and the extraction grids for several radiofrequency (RF) powers and mass flow rates. Measurements in iodine are compared to xenon, krypton and argon in order to evaluate performances of these various propellants for ionization (and therefore power) efficiency. At low mass flow rates, iodine is found to be the most efficient propellant, however, as the mass flow rate increases, the ionization cost in iodine increases rapidly due to both its molecular and electronegative nature. The ratio of negative ion to electron density is measured using laser-induced photodetachment in order to quantify the effect of iodine electronegativity. Finally, all measurements are compared to a previously published global (volume-averaged) model. The agreement between model and experiments is acceptable, however several modelling improvements are proposed.

1. Introduction

Plasma thrusters are now routinely used on both space missions and commercial satellites. Most of current thrusters use xenon as the propellant. However, iodine is being studied by several groups around the world [1, 2, 3, 4, 5, 6, 7, 8, 9] as an alternative to xenon. Xenon hegemony is mainly questioned for its cost, its scarcity, and its need for a compressed gas handling. Iodine, is solid at standard temperature and pressure, abundant on earth and thus, inexpensive. While massively contained in seawater (approximatively 35 million tons) but with a very low concentration, iodine is mostly extracted from underground brines in Japan, USA, Turkmenistan, Azerbaijan, Indonesia or from caliche ore (a nitrate found in the Atacama desert) in Chile [10, 11]. It is estimated that the iodine reserves of Japan and Chile represent 90% of the world reserves (65% for Japan and 25% for Chile). Iodine is, for instance, mostly needed in the production of X-ray contrast media or in polarizing film in liquid-crystal display

(LCD) screens. It is estimated that the existing global reserves of iodine will support iodine production for at least the next two centuries [10, 11].

In the plasma (electric) propulsion community, iodine has been considered for almost two decades, mainly because of its high mass and its low ionization energy, two key parameters for a good thrust-to-power ratio. However, iodine has not yet convinced the major industrial manufacturers. The main reluctance to use iodine stems from its corrosive nature as well as the costs generated by the adaptation of industrial ground testing facilities operating exclusively with noble gases. Nevertheless, *Busek*® is already marketing Hall effect thrusters fueled by iodine, and *ThrustMe*® recently reported promising in-orbit performances of their iodine electric propulsion system [5].

Even if xenon and iodine thrusters performances are found to be very similar [5, 12], iodine and xenon plasmas should exhibit very different properties, in particular as the mass flow rate (and the resulting gas pressure in the plasma chamber) and the electric power used to generate the plasma are varied. Iodine is a molecular and electronegative gas, which is expected to have a higher energy cost per electron-ion pair created, because of the energy cost of dissociation and vibrational excitation. A significant fraction of negative ions is also expected given the very high cross section for dissociative attachement. Furthermore, transport phenomena are also different in molecular gases, and the electron energy relaxation length is expected to be shorter in iodine than in noble gases. All the above effects remain to be quantified and there is a lack of both basic data (cross sections, transport coefficients, etc.) and relevant literature at very low pressure. Accurate diagnostic techniques, both optical and electrical, are therefore necessary to quantify the plasma properties and guide the development of reliable models [6, 9]. This will be the first step towards the optimization of propulsion devices, both for gridded ion thrusters [4, 13] and/or Hall thrusters [1, 12].

On the diagnostics side, this paper focuses first on charged-particles measurements. Spatially resolved Langmuir probe measurements are used to record the electron density and electron energy distribution variations away from the powered antenna. These measurements provide useful information on the ionization efficiency and on the electron transport phenomena. Langmuir probe measurements had already been performed in the same setup in argon [14] and SF_6 [15] discharges, both with and without magnetic filter, and preliminary measurements were taken in iodine discharge and reported in two Ph.D. theses [16, 17]. In this paper we investigate mass flow rate (pressure) and discharge power effects in iodine, along with a detailed comparison of iodine with the noble gases (xenon, krypton and argon) in the regime of interest for plasma propulsion.

The second objective of this work is to study the electronegativity (ratio of the negative ion density to the electron density) of iodine plasmas. Early works have shown that iodine is a very electronegative gas [18, 19], with electronegativity values well above unity. Woolsey *et al.* used a Langmuir probe and orbital-limited theory and found electronegativity values above two thousands in a nearly ion-ion plasma (I_2^+-I_3^-), produced by allowing the plasma produced in the Faraday dark space of a DC iodine glow discharge to diffuse into a side-arm for pressures between 0.2 and 1 Torr [20]. More

recently, Grondein [16] applied the procedure developed by Bredin *et al.* [21] to iodine plasmas and deduced electronegativity values above a thousand near the exhaust grid of the PEGASES thruster when a magnetic field was applied at 1 mTorr. Here we use laser induced photodetachement [22] to measure the electronegativity in a large range of parameters. Spatially resolved electronegativity measurements will be presented. Combined with Langmuir probe measurements, the photodetachment measurements give the negative ion and positive ion density profiles in the iodine plasma chamber. One important finding is that negative ions are not in Boltzmann equilibrium, an assumption often used in Langmuir probe theories of electronegative plasmas [23, 21].

Finally, the experimental results are compared to a previously published global (volume-averaged) model of an iodine ion-gridded thruster[6]. Six species are considered in the model: I, I_2, I^+, I_2^+, I^- and e^-. The comparison shows that the model is in reasonable agreement with experiments but it also helps to identify ways to improve the modelling.

The present paper is organized as follows. First, the experimental apparatus is described in Section 2. The Langmuir probe measurement procedure and the laser photodetachment technique are presented in Section 3 and in Appendix A, while results are discussed in Section 4. The global model is briefly presented (with a detailed presentation of the model equations in Appendix B) before being discussed and compared to experimental measurements in Section 5. Conclusions are given in Section 6.

2. Experimental apparatus

Measurements were performed in the so-called PEGASES thruster setup, described in details in previous publications [21, 16, 17]. In the present study, the magnetic barrier and acceleration stages are removed. The plasma chamber is a rectangular cuboid of 1.25 L (8 cm x 12 cm x 13 cm inner dimensions), with aluminum grounded walls and a single grounded aluminum grid (7 cm x 11 cm) at the exhaust plane. The geometrical grid transparency is around 10 %.

The plasma chamber is connected to a 50 L spherical vacuum chamber pumped by a turbo-molecular pump backed by an oil-free scroll pump, shown in Figure 1. The vacuum lower limit, when no gas is injected, is around 10^{-4} mbar $\sim 7.5\times10^{-2}$ mTorr (0.01 Pa). Iodine is injected through a MKS 1150C-4805M mass flow controller calibrated for 50 sccm of I_2 . All pipes in the injection line are heated before and during operation to avoid deposition and clogging. Exhausted iodine is captured by a liquid nitrogen cold trap located between the turbo-molecular pump and the scroll pump. A movable arm, holding the electrical probes (further detailed), allows to scan 10 cm-long spatial variations inside the discharge. The probe goes through the exhaust grid thanks to a centered 1 cm diameter hole. Experiments were performed at fixed pressure and discharge power adjusting respectively the mass flow rate and the power delivered by the generator. The ferrite and the antenna are cooled down by circulating cold water.

When the plasma is turned on, the reactor wall temperature varied between 300 and 330 K depending on the plasma conditions.

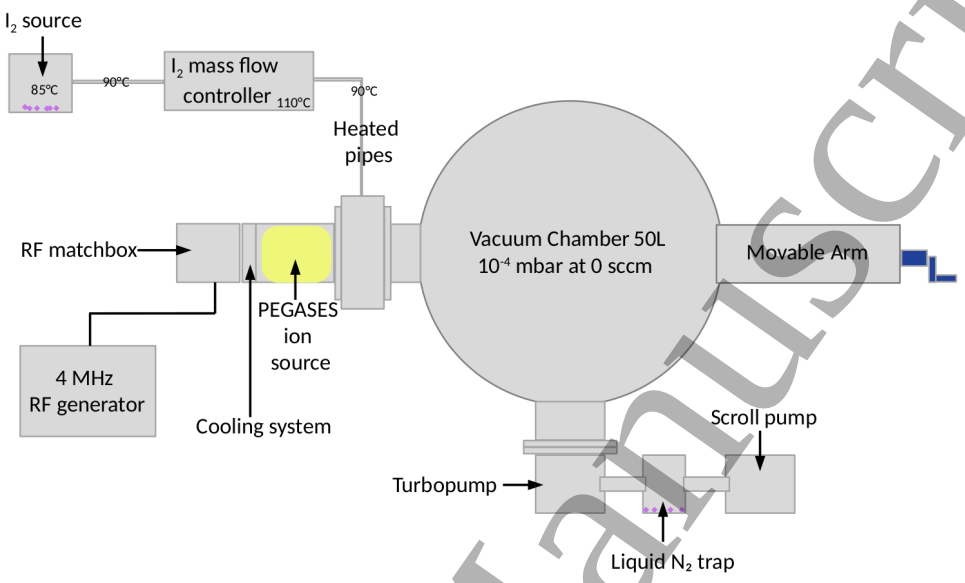

Figure 1. Experimental setup schematics. A liquid N_2 trap captures iodine through condensation before it reaches and damages the scroll pump. Slightly adapted from [17].

Iodine radio-frequency inductively coupled plasmas can be generated at pressures ranging from 0.3 to 30 mTorr (0.04 to 4 Pa), using argon to ease ignition. The gas pressure is monitored with a capacitance manometer 627D Baratron from MKS. The plasma is generated using a 4 MHz RF generator (RFPP RF25M), the matchbox is custom made and the coil antenna is a flat antenna inserted in ferrite as described elsewhere [24]. The pressure - absorbed power characteristics of the experiment is presented in Figure 2. The discharge power values reported are the actual power absorbed in the plasma, calculated using the method of Godyak *et al.* [25] to subtract any power dissipated in the electrical components of the match box and coil antenna. It is not possible to ignite a plasma at low power and the breakdown power region is indicated in red. The yellow region is the region investigated in this work. The maximum achievable power is indicated in black. The experimental setup would be damaged if operated at higher power. The width of both limit regions is only indicative and subject to hysteresis.

Argon, krypton and xenon discharges may also be generated with the same setup but using independent mass flow controllers and injection lines (not represented in Figure 1). Given the mass flow controller ranges, xenon plasmas can be obtained between 0.3 and 3.5 mTorr, krypton plasmas between 0.3 to 2.5 mTorr and argon plasmas between 1 to 15 mTorr. The power range that can be explored with noble gases is between 50 W and 300 W.

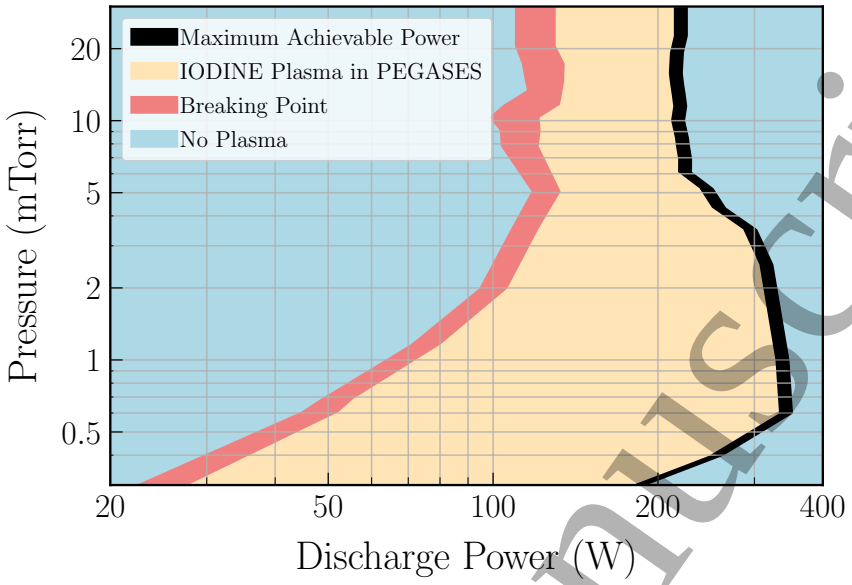

Figure 2. Pressure (mTorr) versus Discharge Power (W) characteristics of the experimental setup working on iodine. The pressure can be varied from 0.3 mTorr to 30 mTorr (0.04 to 4 Pa).

3. Diagnostics

3.1. Langmuir probe

The Langmuir probe design is presented in Figure 3a. It consists of two tungsten wires of 100 μm inserted in a bi-holed 15 cm long ceramic tube with an external diameter of 1.5 mm. The first wire is used as the Measuring Probe (MP) and the other wire is used as a Reference Probe (RP). The probes are 3.5 mm long. The probe is mounted on a movable arm (see Figure 1) in order to scan the axial position in a 10 cm range, from $z = 1.5$ cm to $z = 11.5$ cm. The alumina window located in front of the inductive coil (antenna) is at $z = 0$ cm (see Figure 3b) while the exhaust grid is located at $z = 13$ cm.

Data are acquired using the Multifunction Plasma Probe Analyser (MFPA) from *Plasma Sensors*®. The MFPA takes advantage of the RP to compensate for plasma potential drifts or fluctuations. The probe is cleaned by ion bombardment between each scan (a negative bias is imposed to the probe). The Druyvesteyn method [26] is used to measure $f(\varepsilon)$, the Electron Energy Probability Function (thereafter designated EEPF in [eV$^{-3/2}$m^{-3}]), by double differentiation of the collected electronic current $I_e(V)$:

$$\frac{\mathrm{d}^2 I_e}{\mathrm{d}V^2} = \frac{e^2 S_\mathrm{p}}{4}\sqrt{\frac{2e}{mV}}F(\varepsilon) = \frac{e^3 S_\mathrm{p}}{2\sqrt{2m}}f(\varepsilon)\ , \tag{1}$$

where $F(\varepsilon) = \varepsilon^{1/2} f(\varepsilon)$ is the Electron Energy Distribution Function (EEDF in [eV^{-1} m^{-3}]) and S_p the probe surface. The electron density n_e [m^{-3}] and the effective electron temperature $T_e = \frac{2}{3}\langle\varepsilon\rangle$ [eV] are then obtained by integration of the distribution over

energy:

$$n_e = \int_0^{+\infty} \varepsilon^{1/2} f(\varepsilon)\, \mathrm{d}\varepsilon \ , \tag{2}$$

$$T_e = \frac{2}{3} n_e^{-1} \int_0^{+\infty} \varepsilon^{3/2} f(\varepsilon)\, \mathrm{d}\varepsilon \ . \tag{3}$$

The Druyvesteyn method [26] has been preferred to the usual Langmuir method [27] because recent works from Godyak [28, 25] evidenced some limits of the later procedure. Note that the ion current has not been subtracted to the probe current because of the issues underlined in [29, 25].

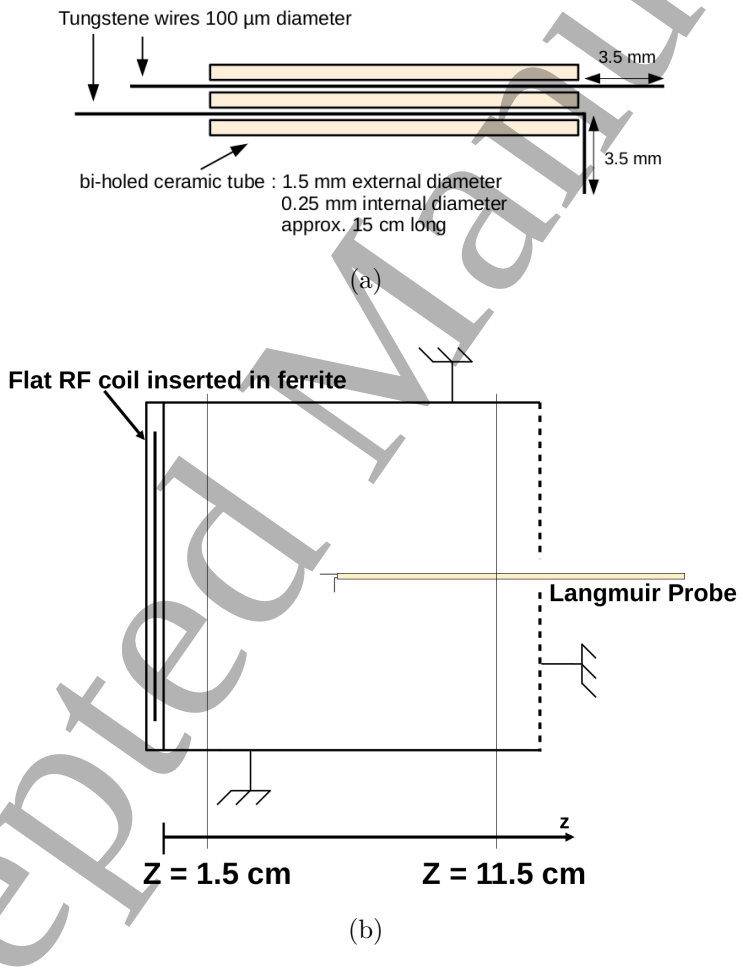

Figure 3. (a) Langmuir probe design and characteristics. (b) Insertion of the Langmuir probe inside the ICP chamber. The probe goes through the exhaust grid and can scan the plasma from $z = 1.5$ cm to $z = 11.5$ cm, the axis origin being the ferrite location. Internal walls and the exhaust grid are grounded.

Probe signals were corrected using the procedure described by Godyak in [25] and detailed in Appendix A. The correction modified the results up to +20% for n_e and -15% for T_e in the highest pressures in iodine, where very strong spatial gradients have been observed and contamination of the probe is expected to be the greatest.

Contamination of the discharge walls may also lower the conductive properties of the surfaces and affects the return current. Finally, the repeatability of the Langmuir probe measurements has been checked by reproducing the same plasma conditions with several probes on different experimental campaigns (over several months), and the error in the measured electron density and temperature was less than 15% (error bars have not been plotted in Section 4).

3.2. Laser induced photodetachment

3.2.1. Principle and experimental setup In our experimental conditions, I^- is likely to be the dominant negative ion. It is produced by dissociative attachement (DEA) on molecules:

$$I_2 + e^- \longrightarrow I^- + I \, . \tag{4}$$

Previous works in high pressure iodine discharges [30] also detected I_3^- and I_2^- negative ions, but in small amount compared to I^-. The measurement of the electronegativity α, defined as the ratio of the negative ion density n_{I^-} over the electron density n_e, is carried out using the laser-induced photodetachment technique, developed in hydrogen plasmas by Bacal in the late 1970's [31]. The technique is adapted here for iodine plasmas. The experimental setup and typical signals are shown in Figures 4-5.

A Nd-YAG ns-laser from Quanta-Ray is tripled to obtain a laser beam at 355 nm able to photo-detach the electrons from I^- (photon energy: $h\nu = 3.49$ eV $> \varepsilon_A = 3.0590463$ eV, the electron affinity [32]), according to the following process:

$$I^- + h\nu \longrightarrow I + e^- . \tag{5}$$

The optical setup used is presented in Figure 4b. Four mirrors from Opto4U with a R_{max} at 45° for wavelengths between 351 and 355 nm were used to eliminate residual light at 532 and 1064 nm. The laser energy was modified using a 25.4 mm diameter half-wave plate at 355 nm from Optoprim and a polarizer cube from Lambda Research Optics (HPB-25-4U-355): in this way, the beam shape was not modified when the energy was changed. The laser energy was measured after passing through the plasma chamber.

The newly created electrons are captured by using a 200 μm diameter and 3 mm-long tungsten probe (see Figure 4a) which is biased above the plasma potential and located at the center of the laser beam. The probe is inserted inside the plasma and can move from $z = 1$ cm to $z = 11$ cm, along with the laser beam (by using a movable mirror; see Figure 4b). However, due to limited optical access through the lateral windows, the spatial scan was only done from $z = 1$ cm to $z = 9.7$ cm.

By using the electrical circuit shown in Figure 5a, the time-varying current collected by the probe (triggered on the laser pulse) was separated from the DC current to the probe. The typical time-varying signal is shown in Figure 5b. After the laser pulse, a current pulse (due to photo-detached electrons) is collected on the probe and lasts a few micro-seconds before the relaxation to equilibrium. Bacal [31, 22] showed that the electronegativity is equal to the ratio of this current pulse over the DC current. Given

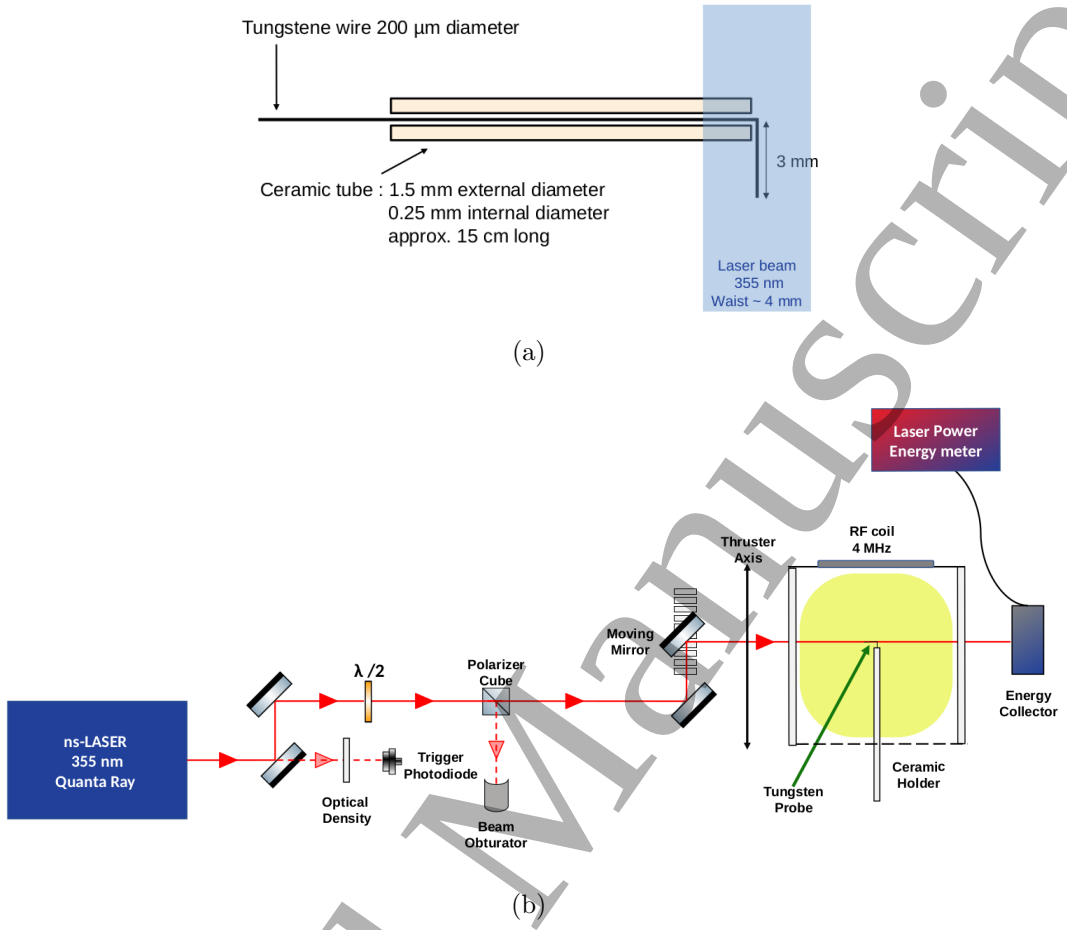

Figure 4. (a) Photodetachment probe design and characteristics. The laser beam is represented in blue. (b) Optical setup for the laser photodetachment with the laser beam in red.

our electrical circuit, we have:

$$\alpha = \frac{\Delta j_{e_{\mathrm{AC}}}}{j_{e_{\mathrm{DC}}}} = \frac{47}{(47\times 50)/(47+50)} \frac{\Delta V_{e_{\mathrm{AC}}}}{V_{e_{\mathrm{DC}}}} = 1.94 \frac{\Delta V_{e_{\mathrm{AC}}}}{V_{e_{\mathrm{DC}}}}, \tag{6}$$

where the voltages are measured on an oscilloscope.

3.2.2. Saturation analyses The photodetachment signal must saturate with both the laser beam energy and the potential applied to the probe. The theoretical photodetachment fraction is a function of the photodetachment cross-section σ and the laser energy E_{Laser}, according to

$$\alpha = \alpha_0 \left(1 - \exp\left(-\frac{\sigma}{S}\frac{E_{\mathrm{Laser}}}{h\nu}\right)\right), \tag{7}$$

where α_0 is the electronegativity of the probed area (reached at saturation), and S the laser beam surface [31, 22]. In our experiments, $S = \frac{\pi}{2}w^2 \approx 0.25$ cm^2 (laser beam waist w of 4 mm). Saturation with respect to the laser energy is shown in Figure 6a for a fixed position ($z = 9$ cm) at 0.75 mTorr and 100 W, and the probe biased at +40 V. The

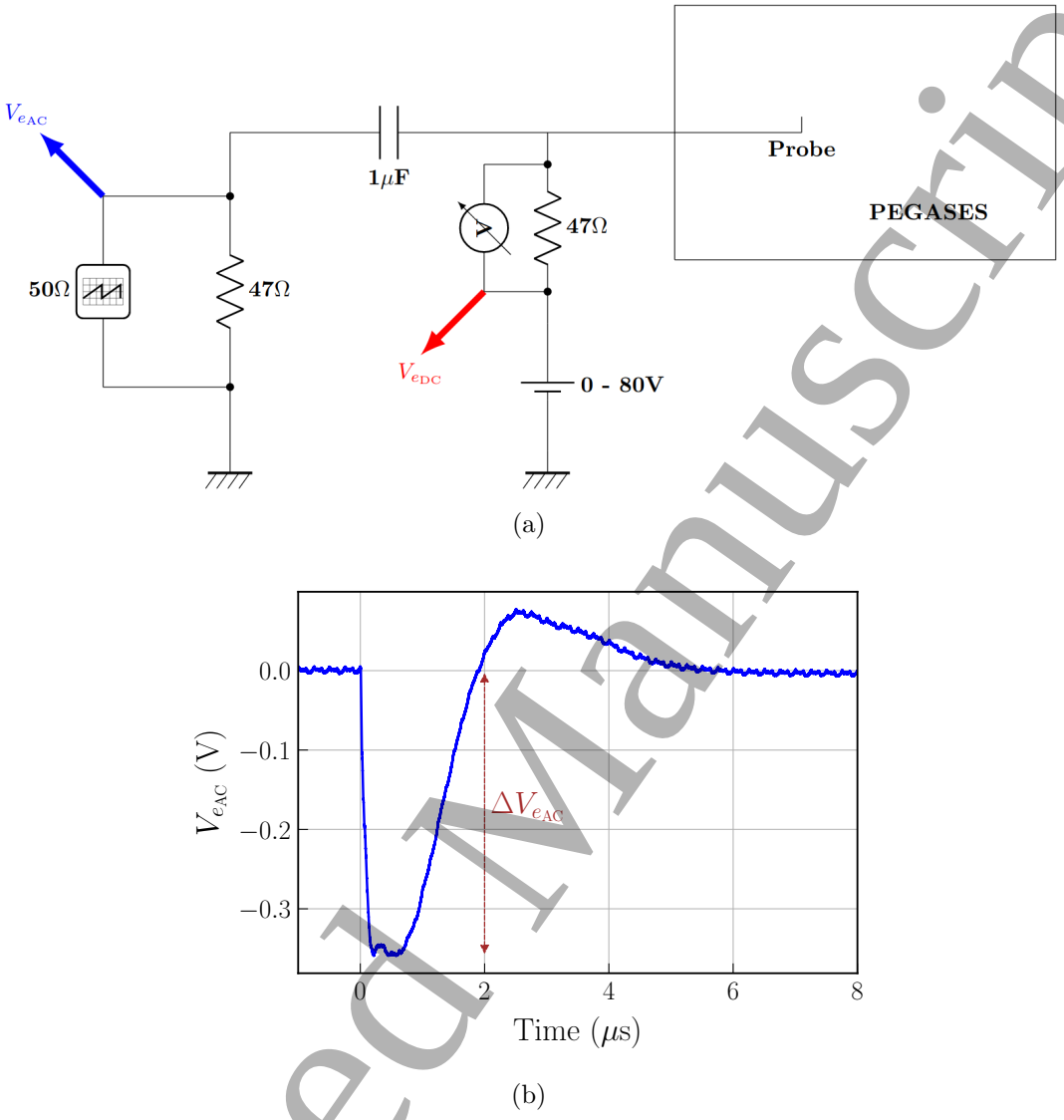

Figure 5. (a) Electrical circuit used to separately collect the alternative and the direct current from the photodetachement probe. (b) Typical alternative photodetachment signal obtained for a pressure of 1.5 mTorr and a discharge power of 100 W at $z = 3$ cm from the antenna. In this situation, $\Delta V_{e_{AC}} = 0.36$ V and $V_{e_{DC}} = 5.22$ V: the resulting electronegativity is close to 0.134.

experimental data are fitted using equation 7, α_0 and σ being the fitting parameters. A photodetachment cross-section of 2×10^{-17} cm^2 is retrieved, in agreement with the measured value for I^- at 3.49 eV [33], which confirms our assumption on the dominant negative ion. However, note that although the laser wavelength used here was larger than the threshold for I_3^- (4.226 eV threshold [34]), it was short enough to photodetach electrons from I_2^- (2.524 eV threshold [35]). Consequently, even if we are confident that I^- is the dominant negative ion, we could not formally exclude the presence of I_3^- which would not be detected by our diagnostic.

The voltage applied to the probe has to be high enough to collect all the photo-

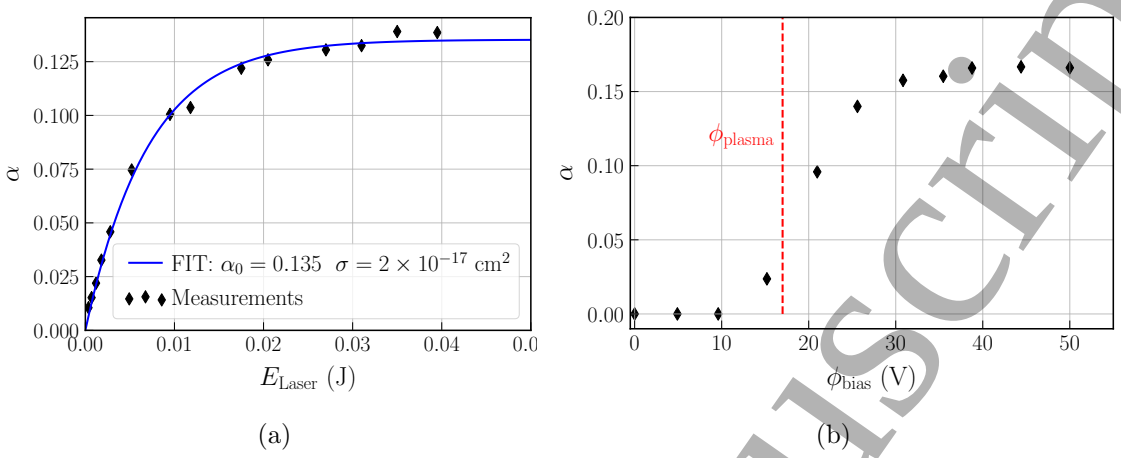

Figure 6. (a) Saturation analysis with the laser energy for a fixed bias voltage of 40 V. Experimental data were taken at $z = 9$ cm for a pressure of 0.75 mTorr and a discharge power of 100 W. The saturated electronegativity α_0 and the photodetachement cross-section σ are inferred by fitting with equation (7). (b) Saturation analysis with the bias voltage of the probe for a fixed laser energy of 40 mJ. Experimental data were taken at $z = 5$ cm for a pressure of 0.65 mTorr and a discharge power of 50 W. The plasma potential ϕ_{plasma} is indicated in red and measured using the Langmuir probe.

detached electrons. A saturation analysis with respect to the probe bias is presented in Figure 6b. Data were acquired at $z = 5$ cm for a pressure of 0.65 mTorr and a discharge power of 50 W. In this case, 35 V was enough to collect more than 95% of the detached electrons. This voltage is significantly above the plasma potential and the probe could therefore perturb the plasma. It was checked, by using a floating probe located only a few millimeters away from the measuring probe, that the floating potential was never significantly affected by this large bias.

The saturation analyses were done at each operating conditions that are reported here. While a laser energy of 40 mJ was enough in all conditions, the bias voltage had to be adjusted when pressure was increased because of the change in plasma potential and the strong spatial gradients. For instance at $p_{\text{neutrals}} \geq 10$ mTorr, where strong spatial gradients of the electron density were evidenced (see Figure 10a) and the electron density was greater than 10^{18} m^{-3} near the antenna, the bias voltage had to be increased up to 55 V in order to reach saturation.

Finally, photodetachment measurements were repeated several times over several days and the observed variations in the electronegativity never exceeded $\pm 10\%$.

4. Results

4.1. Iodine versus noble gases

We start our investigation by comparing iodine and nobles gases plasma properties in typical operating conditions of electric propulsion (pressure below 3 mTorr and discharge

power of 100 W). Figure 7 shows the spatial variations of electron density and electron temperature in iodine, xenon and krypton plasmas at 0.5 mTorr and a discharge power of 100 W. For the three gases, the well-known features of very low pressure ICP discharges are retrieved: electrons are isothermal because of highly non-local electron kinetics (Figure 7b) and the electron density profiles have a quite flat but dome-like shape (Figure 7a) [36]. It has also been found that doubling the discharge power roughly doubles the electron density, and only weakly affects the electron temperature.

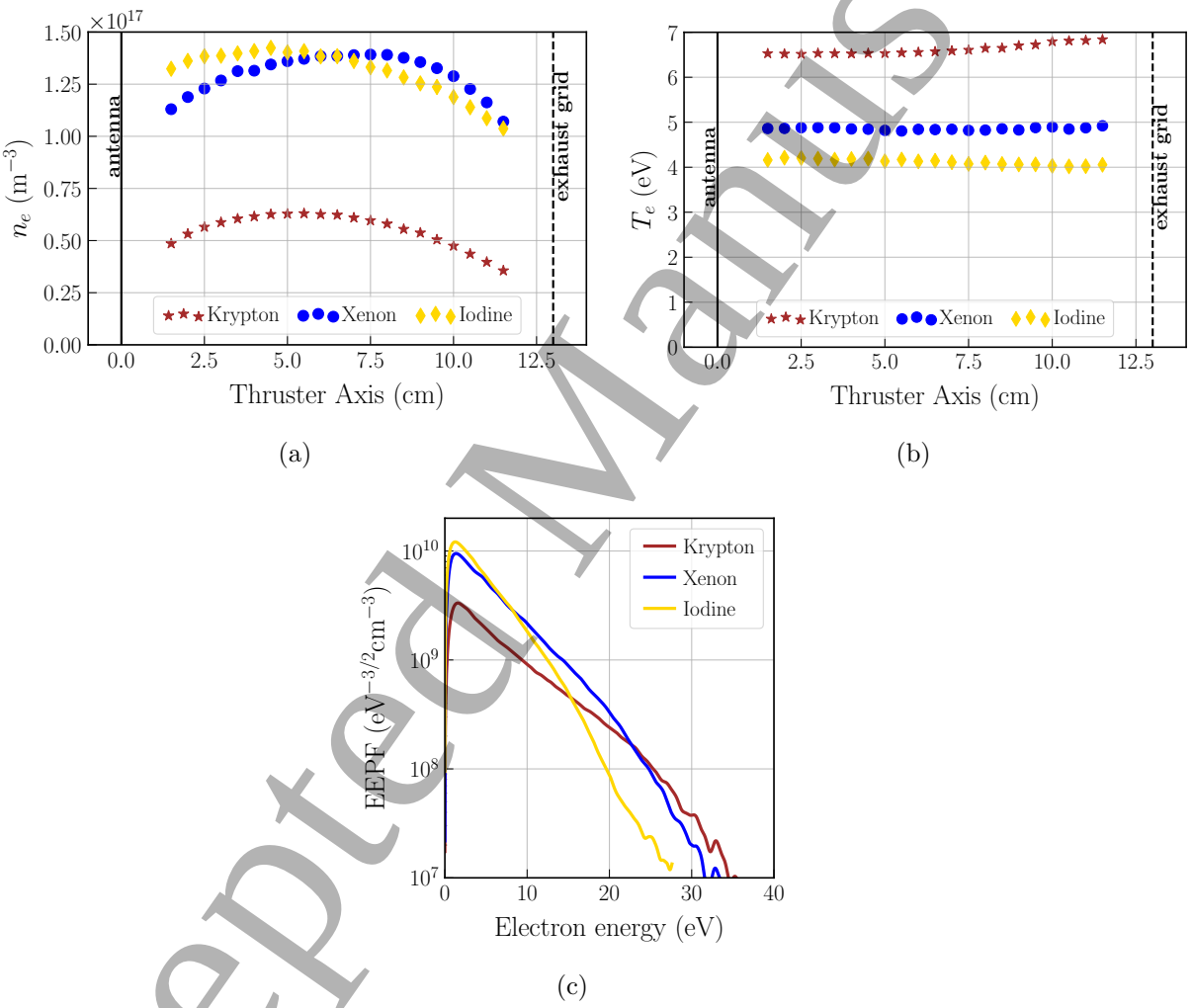

Figure 7. Langmuir probe measurements in iodine, xenon and krypton plasmas for a pressure of 0.5 mTorr and a discharge power of 100 W. (a) Spatial profiles of the electron density n_e (m^{-3}) along the thrust axis. (b) Spatial profiles of the electron temperature T_e (eV) along the thrust axis. (c) Measured EEPF at $z = 6.5$ cm.

As it can be seen, the electron density in iodine and xenon are very close with a maximum around 1.5×10^{17} m^{-3}. We note, however, that the density maxima are not located at the same position, with a slight localisation near the antenna in iodine (that will be observed more clearly at higher pressures). This observation suggests that the energy relaxation length [37] is shorter in iodine, which could be explained by the

additional energy loss channels in a molecular plasma. The electron temperature is lower in iodine than in xenon which is expected since the ionization energy of atomic and diatomic iodine ($\varepsilon_{\mathrm{iz,I}} = 10.45$ eV, $\varepsilon_{\mathrm{iz,I_2}} = 9.31$ eV) are lower than that for xenon ($\varepsilon_{\mathrm{iz,Xe}} = 12.1$ eV). Krypton electron density values are at least twice lower than in xenon and iodine. This confirms that krypton is not as efficient as xenon and/or iodine to achieve large plasma densities. The higher ionization energy of krypton ($\varepsilon_{\mathrm{iz,Kr}} = 14.0$ eV) explains this lower efficiency, as well as the higher electron temperature of 6.5 eV. The ionization energies are taken from the NIST website [38].

The EEPF recorded at $z = 6.5$ cm are shown in Figure 7c. They are mostly Maxwellian at low energies and a significant depletion is seen well above the first excitation energies. As already reported in argon discharges [39], this is because the major electron energy loss mechanism in the low pressure (free fall) regime comes from fast electrons escaping to the wall. The depletion in iodine arises at lower energy than with noble gases, both because the sheath potential is lower (because T_e is lower), and because the excitation energies are lower. Note that the EEPF in krypton also exhibits a peak at low energy, already observed in argon, and typical in ICP at low gas pressure [25, 39].

To summarize, at low pressure (0.5 mTorr) and sufficiently high discharge power, iodine plasmas appear as efficient as xenon to achieve high density plasmas. In these conditions, the iodine plasma is turquoise and is probably highly dissociated ($n_{\mathrm{I_2}} \ll n_{\mathrm{I}}$). A significant fraction of molecules would lead to a strong emission in the range 500-600 nm (yellow color). The dominant species are expected to be I^+, e^- and I. Since negative ions are produced by dissociative attachment, the negative ion density is expected to be low.

We now examine the results shown in Figure 8, obtained for the same discharge power of 100 W, but at the higher pressure of 2.5 mTorr. As before, the electron density (8a) and the electron temperature (8b) are plotted versus the distance from the antenna. The EEPF measured at $z = 6.5$ cm are shown in Figure 8c. For these plasma conditions, we add argon measurements to extend the comparison to additional alternative propellants.

Iodine and xenon electron density profiles are now significantly different. Near the antenna, the electron density is about 2.5×10^{17} m^{-3} and the temperature about 3 eV in both gases. However, in the case of iodine, the density is maximal near the antenna and falls off quickly, down to 0.5×10^{17} m^{-3} at $z = 11.5$ cm. On the contrary, the electron density profile in xenon still exhibits a dome-like shape, but with a maximum closer to the antenna at $z = 5$ cm (where $n_e \approx 3 \times 10^{17}$ m^{-3}). The density near the exhaust grid is three times higher than in iodine. The electron temperature is almost constant in xenon, around 3 eV, while in iodine it decays as the distance from the antenna increases. Overall, these results are consistent with the conclusion drawn before; the energy relaxation length must be shorter in iodine, leading to stronger localisation of the discharge where the RF power is deposited, i.e. in the skin depth close to the antenna. The results in krypton and argon are quite similar to that in xenon but with

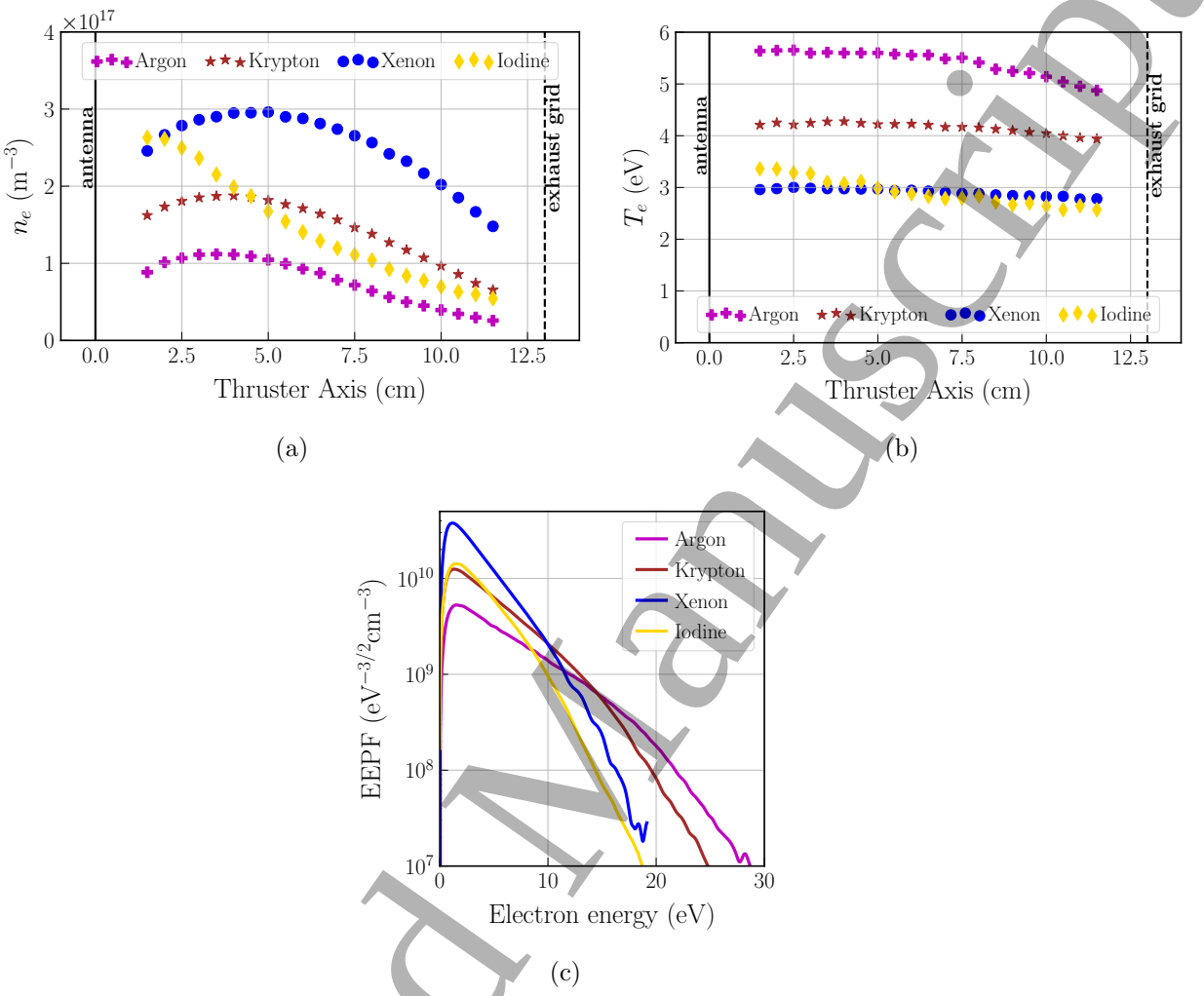

Figure 8. Langmuir probe measurements in iodine, xenon, krypton and argon plasmas for a pressure of 2.5 mTorr and a discharge power of 100 W. (a) Spatial profiles of the electron density n_e (m^{-3}) along the thrust axis. (b) Spatial profiles of the electron temperature T_e (eV) along the thrust axis. (c) Measured EEPF at $z = 6.5$ cm.

lower electron densities and higher electron temperature, in agreement with the higher ionization potential of these noble gases ($\varepsilon_{\mathrm{iz,Ar}} = 15.76$ eV [38]). The EEPFs are shown in Figure 8c. The conclusions drawn at 0.5 mTorr stay true but the low energy peak is less pronounced in krypton.

To summarize this comparison between iodine and noble gases and draw conclusions on the relative efficiency for electric propulsion applications, the electron density measured in the center of the discharge ($z = 6.5$ cm) is plotted as a function of the discharge power in Figure 9 for two pressures: 0.6 mTorr and 2.5 mTorr. Efficiency of a plasma thruster may be defined in different ways. A way to evaluate this is to calculate the thrust-to-power ratio, usually defined in the rocket engineer community has the thrust in mN, divided by the power in kW. In a Gridded-Ion-Thruster, the thrust is proportional to the ion flux, and therefore to the plasma density. The power is the

sum of the thrust power and the power absorbed to generate the plasma. It becomes then clear that to maximize the thrust-to-power ratio, ones needs to reach the highest plasma density for the smallest power required to generate the plasma. Langmuir probe measurements indeed evaluate the plasma density for a given absorbed power.

In light of the above, one could state the following: (i) at low pressure (and therefore mass flow rates) and for a sufficient input power, iodine appears to be comparable or even slightly more efficient than xenon, (ii) as soon as the pressure (and/or the mass flow rate) increases, xenon appears more suitable. This could be expected and comes from the electronegative and molecular nature of iodine. (iii) Because of a high ionization energy and a lower mass, argon is not competitive. Krypton is less efficient than xenon, but it could be a good compromise at large mass flow rates since it is less expensive than xenon.

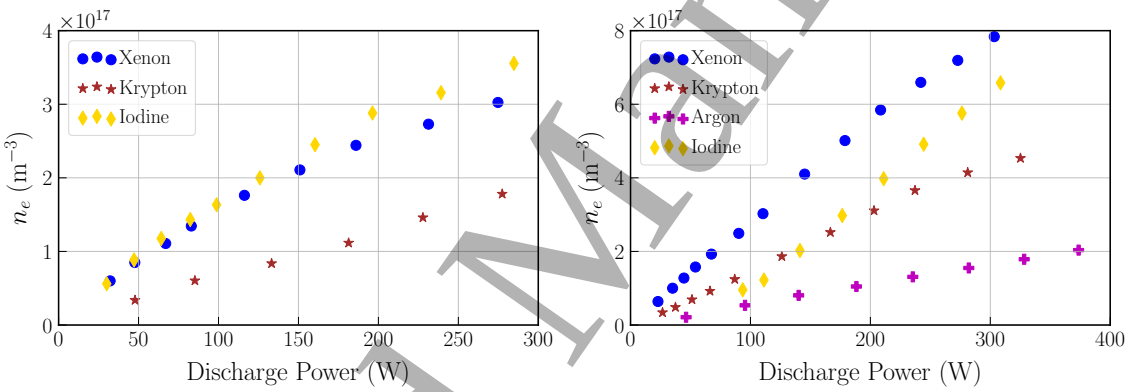

Figure 9. Electron density n_e (m^{-3}) versus discharge power (W) in PEGASES thruster operating with iodine, xenon, krypton or argon. Measurements were taken at $z = 6.5$ cm using a Langmuir probe. (a) 0.6 mTorr. (b) 2.5 mTorr.

4.2. Additional Langmuir probe results in iodine plasmas

Iodine plasmas have been investigated in a larger parameter space, in order to better capture the transition to higher pressure regimes, and construct a large data base for future comparisons with numerical simulations. Langmuir probe measurements have been performed at fixed discharge power (200 W) and the pressure was varied from 0.5 mTorr to 15 mTorr. Results are shown in Figure 10.

The density peaks near the antenna as the pressure increases (see Figure 10a). At 15 mTorr, the electron density reaches up to 1.5×10^{18} m^{-3} at $z = 1.5$ cm, and then strongly decreases down to 4×10^{16} m^{-3} at $z = 11.5$ cm. The plasma is almost stratified. In the antenna region, the electron density increases with pressure, while in the extraction region, typically for $z > 6$ cm, the electron density decreases with pressure. Increasing the pressure also introduces significant gradients in the electron

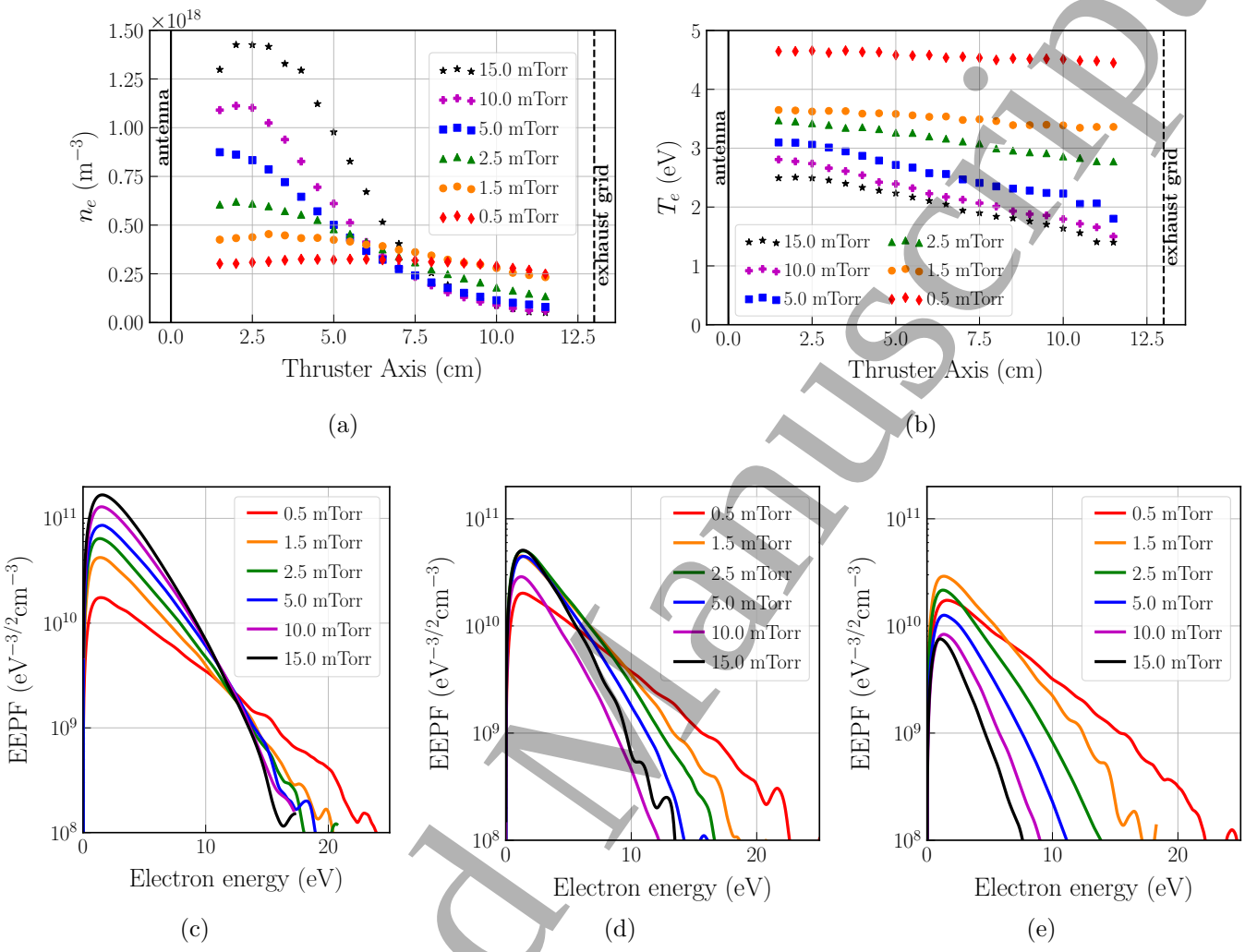

Figure 10. Langmuir probe measurements in a purely iodine plasma for a discharge power of 200 W and pressures from 0.5 mTorr to 15 mTorr. (a) Spatial profiles of the electron density n_e (m^{-3}) along the thrust axis. (b) Spatial profiles of the electron temperature T_e (eV) along the thrust axis. Measured EEPF at: (c) $z = 1.5$ cm, (d) $z = 6.5$ cm, (e) $z = 11.5$ cm.

temperature (see Figure 10b). At 0.5 mTorr, the temperature drops by only 0.2 eV, with a mean of 4.5 eV. At 15 mTorr, the temperature drop is nearly 1.2 eV for a mean temperature of 2 eV. For completeness, the EEPFs are plotted in Figures 10c, 10d and 10e for three different locations ($z = 1.5$ cm, $z = 6.5$ cm and $z = 11.5$ cm). The electron cooling and density gradients are clearly seen, without drastic change in the distribution shapes.

Finally, it is interesting to underline some key characteristics of the experimental results in iodine for the comparison with global models in section 5. At very low pressure ($\lesssim 1$ mTorr), the electron temperature is uniform and the electron density gradients are modest. This regime is particularly adapted for global modelling. For low-intermediate pressures (1 mTorr $\leq p_{\text{neutrals}} \leq 3$ mTorr), gradients become non negligible and global

modelling is expected to partially fail. For higher pressures (> 3 mTorr), gradients are too stiff and global modelling will not be appropriate. Results for $p_{\text{neutrals}} \geq 3$ mTorr show that the localized power deposition (in the skin depth) produces a stratified plasma. The very high electron density near the antenna suggests that iodine is fully dissociated near the antenna and only partially dissociated in the extraction region.

4.3. Electronegativity measurements in iodine plasmas

Electronegativity spatial profiles are shown in Figure 11. Measurements were taken for five different pressures from 0.5 to 15 mTorr and a discharge power of 200 W. At 0.5 mTorr, the electronegativity is very low with a maximum of 0.02 at $z = 5.5$

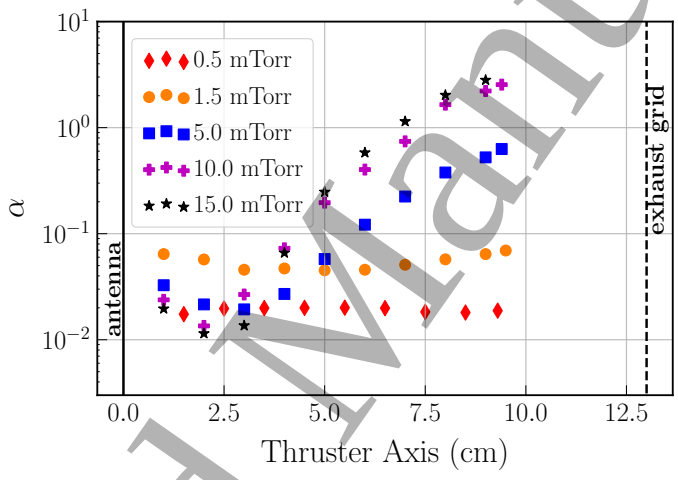

Figure 11. Spatial profiles of the electronegativity α for five different pressures from 0.5 to 15 mTorr and a fixed discharge power of 200 W.

cm. The profile presents a dome-like shape, although it is hardly seen in the log-scale used in Figure 11). In these conditions (large power, very low pressure), the electron temperature is high, the plasma is fully dissociated and the negative ion production by dissociative attachement is very weak (almost no molecules). The plasma is composed mainly of iodine atoms, and is electropositive, which explains that in this case iodine behaves pretty much like xenon (as observed in the previous subsection).

When the pressure is increased, strong gradients appear and the electronegativity profiles always present a minimum in the antenna region. The localization increases as the pressure increases. The electronegativity close to the antenna is only a few percent but reaches almost $\alpha = 3$ at 15 mTorr for $z = 9.5$ cm. The spatial variation of the electronegativity does not follow that of electrons in the sense developed in the next section, in which we show that the negative ion density profiles are inconsistent with a Boltzmann equilibrium. This feature can be explained by a local balance between loss and creation processes of negative ions (see discussion in Section 6).

The influence of discharge power on the electronegativity is studied in Figure 12. The measurements are conducted at a constant pressure of 5 mTorr but for two different discharge powers: 120 W and 200 W. The spatial profiles are presented in Figure 12a. As expected, when the discharge power increases, the electronegativity decreases (the electrons density increases and the I_2 molecules are more dissociated). This is observed at every position. However, Figure 12b shows that the electronegativity ratio (red diamonds) is strongly non-uniform while the electron density ratio (green stars) is almost independent of space. The negative ion density profile is obtained by multiplying the measured electronegativity and electron density profiles. It turns out that increasing the discharge power by a factor of 5/3 decreases the negative ion density by a factor of 4 at $z = 3$ cm, near the antenna, but it barely affects the negative ion density near the exhaust grid. (see Figure 12c). This result strengthens the hypothesis of non-local power deposition, leading to highly non-uniform dissociation processes.

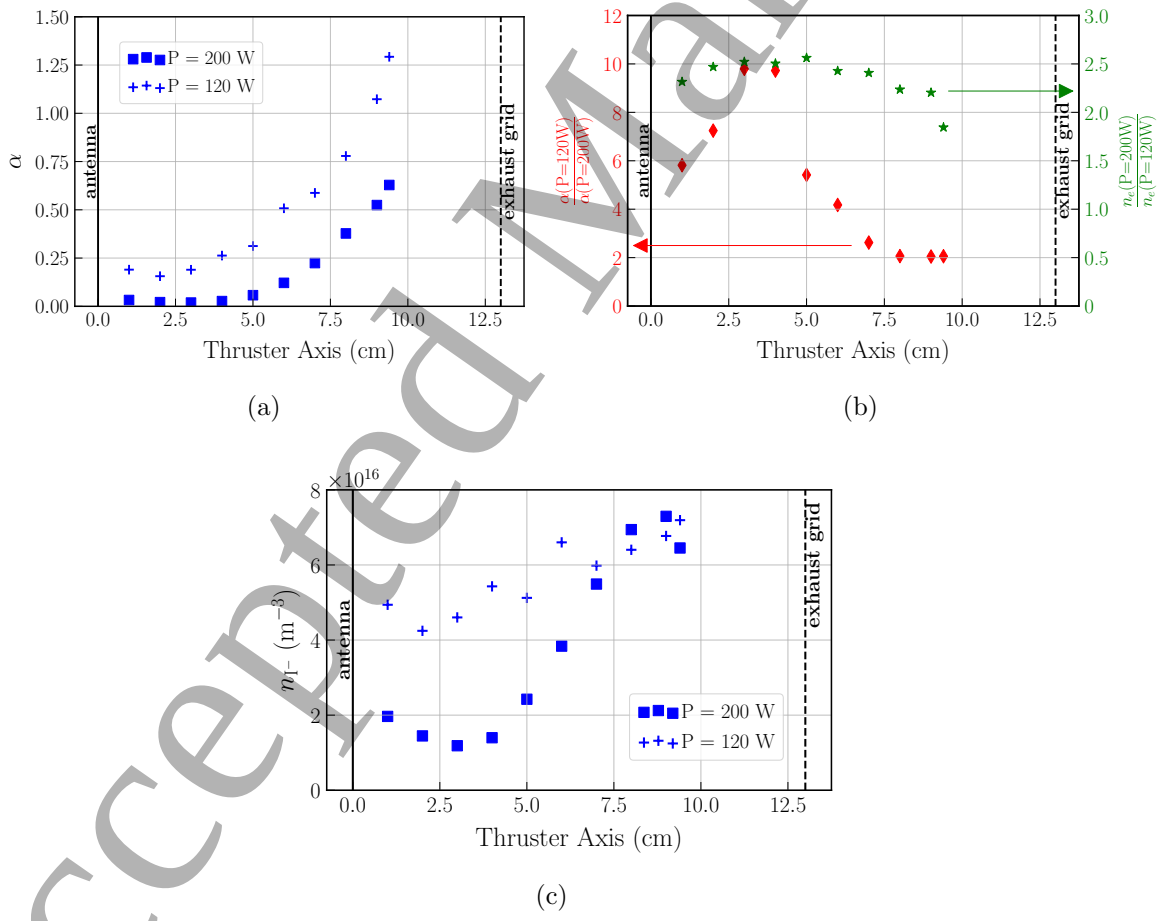

Figure 12. (a) Electronegativity spatial profiles along the thruster axis for a pressure of 5 mTorr and two different discharge powers: 120 W and 200 W. (b) Ratios of the electronegativity and electron density profiles at 5 mTorr and for two different discharge powers: 120 W and 200 W. Note that the discharge power values have been exchanged between α ratio and n_e ratio. (c) I^- density spatial profiles for two different discharge powers: 120 W and 200 W.

To summarize the general idea: at higher pressure the dissociation is higher near the antenna, where the power deposition is localized, leading to very small electronegativity because negative ions are not efficiently produced via dissociative attachment and efficiently destroyed by recombination or electron detachment (because the plasma density is high). Inversely, away from the antenna, the power deposition is negligible, the electron density and temperature are low, and consequently the dissociation is small. This leads to high electronegativity because dissociative attachment becomes very efficient and negative ions destruction inefficient due to lower plasma density.

4.4. Violation of Boltzmann equilibrium

Negative ions are often considered to be in Boltzmann equilibrium in low-pressure electronegative discharges. When collisions and inertial terms are neglected, the momentum equations for electrons and negative ions read:

$$\nabla(n_e e T_e) = -e n_e \mathbf{E}, \qquad \nabla(n_{\mathrm{I}^-} e T_{\mathrm{I}^-}) = -e n_{\mathrm{I}^-} \mathbf{E}, \tag{8}$$

where temperatures are expressed in volts. In 1D and with the isothermal approximation, the system of equations becomes:

$$\frac{\mathrm{d}\phi}{T_e} = \frac{\mathrm{d}n_e}{n_e}, \qquad \frac{\mathrm{d}\phi}{T_{\mathrm{I}^-}} = \frac{\mathrm{d}n_{\mathrm{I}^-}}{n_{\mathrm{I}^-}}. \tag{9}$$

when the electric field is derived from a potential ϕ. Introducing the temperature ratio $\gamma = T_e/T_{\mathrm{I}^-}$, the previous equations become:

$$\gamma \frac{\mathrm{d}n_e}{n_e} = \frac{\mathrm{d}n_{\mathrm{I}^-}}{n_{\mathrm{I}^-}}. \tag{10}$$

Finally, spatial integration gives the electronegativity as a function of the electron density:

$$\alpha(z) = \alpha^0 \left(\frac{n_e(z)}{n_e^0} \right)^{\gamma - 1}, \tag{11}$$

where n_e^0 and α^0 are integration constants at $z = z_0$.
The previous formula, computed using the electron density measurements, is compared to electronegativity measurements at 0.5 mTorr (Figure 13a) and 15 mTorr (Figure 13b) for different values of γ. We chose $z_0 = 1.5$ cm at 0.5 mTorr and $z_0 = 2$ cm at 15 mTorr.

At very low pressure, there is a good agreement between the Boltzmann equilibrium approximation and the actual measurements when $\gamma = 3$. This low value of γ requires that atoms and ions produced from molecular dissociation are very energetic, resulting in temperatures around or above the electron-volt. This seems quite extreme. It is possible that the probe used to collected the electron photo-detached current slightly perturbs the potential. However, negative ions are probably near Boltzmann equilibrium and confined in high plasma potential regions.

However, at 15 mTorr (see Figure 13b), negative ions are clearly not in Boltzmann equilibrium. Whatever the value of γ, the discrepancy between the measured electronegativity and the Boltzmann equilibrium theory exceeds two orders of magnitude

near the exhaust grid even if $T_e = T_{I^-}$. This indicates that negative ions are destroyed by volume processes faster than they can drift in the electric field.

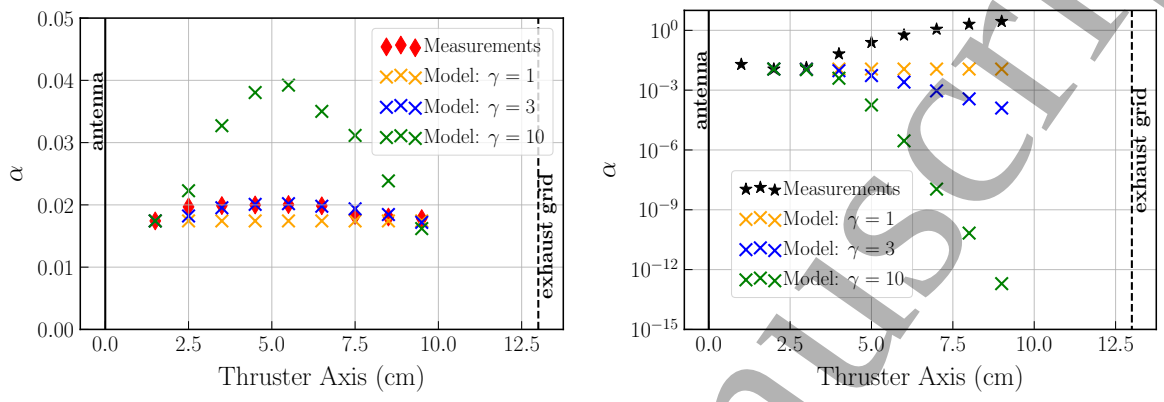

Figure 13. Electronegativity α measured and calculated using Boltzmann equilibrium theory for a discharge power of 200W. In the model, γ is the temperature ratio T_e/T_{I^-}. (a) 0.5 mTorr. (b) 15 mTorr.

4.5. Iodine charged species density profiles

The negative ion density n_{I^-} is derived from the measured electronegativity α and electron density n_e. Then, assuming quasineutrality, one gets the positive density n_+ by adding the electron density and the negative ion density. Here n_+ accounts for all the possible positive ions present in the iodine plasma. Figure 14 shows the charged species density profiles at 0.5 mTorr and 15 mTorr for a discharge power of 200 W.

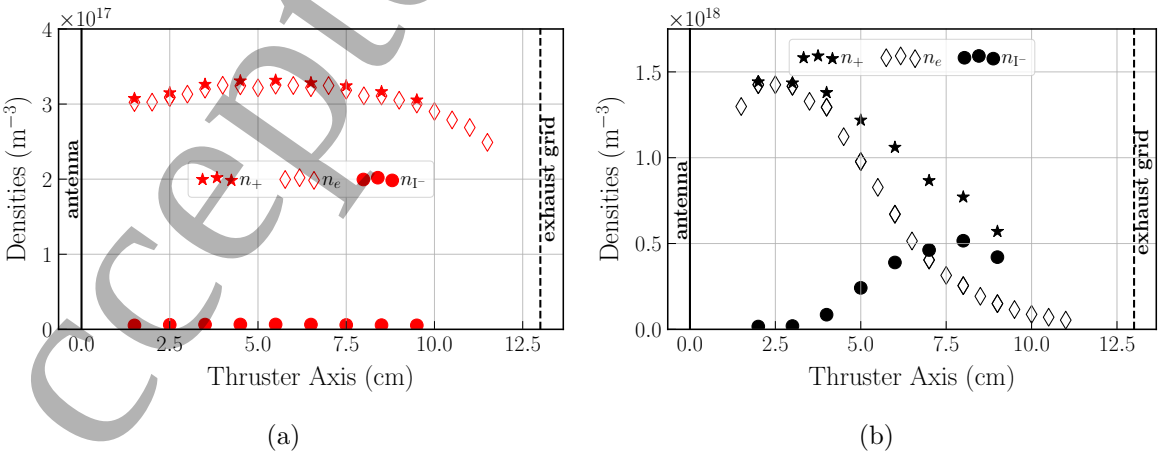

Figure 14. Electron density n_e, negative ion I^- density n_{I^-} and positive density n_+ spatial profiles for a discharge power of 200 W. (a) 0.5 mTorr. (b) 15 mTorr.

At the lowest pressure of 0.5 mTorr (see Figure 14a), it is almost impossible to

distinguish between n_e and n_+, i.e. the negative ion density is negligible. The dominant positive ion species is likely to be I^+, which would explain the similarity between iodine and xenon plasmas for these operating conditions (high power, low pressure). Given the rather low electron temperatures measured in this discharge, no doubly-charged ions are expected to be found. The situation is different at 15 mTorr (see Figure 14b). Near the antenna (and up to $z = 3$ cm), the negative ion density is negligible and $n_e \approx n_+$. However, while the electron density strongly decays away from the antenna, I^- ions gradually become the dominant negative species, with a density maximum around $z = 8$ cm, where $\alpha > 2$. The resulting positive ion density profile decays less abruptly than the electron density profile, which partially explains the observed difference with the xenon plasma case. In this higher pressure case, it is difficult to infer what would be the dominant positive ion. Both I^+ and I_2^+ are likely to be present, with different spatial density profiles. However, the very low electronegativity measured close to the antenna suggests a strongly dissociated plasma and thus that I^+ prevails over I_2^+ in this region.

5. Iodine global model: experimental validation and discussion

The goal of this section is to confront the previous experimental results to an already published iodine global model [6]. The code has been entirely rewritten in the Python language by Marmuse [17] and a parser has been added to automatically generate the ordinary differential equations. This new code has been succesully benchmarked against Grondein *et al.* legacy version [6]. Notations have been slightly modified and aligned to the model descibed in Marmuse Ph.D. dissertation [17]. Previous sections have demonstrated the presence of very strong spatial gradients in both the electron density and the electron temperature (Section 3), as soon as the pressure exceeds 3 mTorr. Since the global model equations are derived for isothermal electrons, the model comparison with experiment will mainly be carried out for pressures below 3 mTorr, for which we assumed isothermal electrons in the plane transverse to the $\hat{\mathbf{z}}$ axis.

5.1. Iodine global model description [6]

The iodine global model used is identical to the one in Grondein *et al.* [6]. Only a brief description of the model is presented here, and the detailed set of equations is given in Appendix B.

The model consists of a cylindrical chamber with an inner radius R and a length L. We let $S_1 = \pi R^2$ and $S_2 = 2\pi RL$ be the surface areas of a closed cylinder. The plasma volume is $V = \pi R^2 L$ and the total surface is $S = 2\pi R^2 + 2\pi RL$. The neutral molecular gas is injected at a fixed rate Q_0 (particle/s). The exhaust grid has an adjustable but constant transparency β_{neutrals} for neutral species and β_{ions} for ions. Generally, because of optical focusing effects, $\beta_{\text{neutrals}} \leq \beta_{\text{ions}}$. The species considered in the model are I atoms, I_2 molecules, I_2^+, I^+, I^- ions and the electrons e^-. Electronically or vibrationally excited states are not considered. Neutral gas heating is included in the model such that T_{I} and

T_{I_2} are dynamic variables. However, note that it was assumed that $T_I = T_{I_2} = T_{neutrals}$. The ions temperatures are all kept constants at 0.1 eV.

The plasma is generated by a circulating RF current with an amplitude of I_{coil} which passes through a coil located around the thruster discharge chamber. The model self-consistently distinguish between the power lost in the coil and the absorbed power by the plasma (the RF power delivered by the generator being the sum of these two powers).

Grondein's work considers a cylindrical thruster while our experiments were conducted in a nearly cubical thruster: it has been decided to keep the same thruster axis length and to adjust the inner radius in order to reach the same internal volume ($V \approx 1.25 \times 10^{-3}$ m^3). To adapt the model to the experimental setup, the RF excitation frequency has been set to 4 MHz and the grid transparency $\beta_{neutrals}$ to 10 %. Since the exhaust grid is not polarized, we have used $\beta_{ions} = \beta_{neutrals}$. All model input parameters are summarized in Table 1.

Table 1. Parameters used in the model.

Thruster	Grid settings	Coil properties	Iodine constants
$R = 5.5$ cm	$\beta_{neutrals} = 0.1$	$\omega = 4$ MHz, $N = 5$	$m_I = \frac{1}{2} m_{I_2} = 126.9$ uma
$L = 13$ cm	$\beta_{ions} = 0.1$	$L_{coil} = 4.84 \times 10^{-6}$ H	$\sigma_{in} = 10^{-18}$ m^2
$T_{wall} = 300$ K		$R_{coil} = 2\ \Omega$	$\kappa_I = 3.9 \times 10^{-3}$ W.m^{-1}.K^{-1}

The list of chemical reactions is presented in Table 2. The fitting parameters for the rate coefficients are given in Table 3, the reaction thresholds are discussed in Appendix A. Most of the rate factors are directly calculated from cross-sections integration assuming a Maxwellian electron distribution (assumption fairly justified by the Langmuir probe measurements in Section 3). The fitting formula reads:

$$K(T_e) = A T_e^{-F} \exp\left(-B/T_e + C/T_e^2 - D/T_e^3 + E/T_e^4\right), \quad (12)$$

where T_e lies in the interval [0.1 eV ; 10 eV]. Unless otherwise stated, the atomic surface recombination rate γ_{rec} is equal to 0.02 as it was proposed in Grondein et al. [6]. Note that this value did not come from a measurement in iodine plasmas, but rather from an analogy to what was measured in chlorine discharges.

5.2. Experimental comparisons

The model inputs are the coil current and the I_2 mass flow rate, while the experimental control parameters are the pressure and the power. In order to compare similar plasma conditions, the model has been run over a very large range of mass flow rates and coil currents to insure that we could find cases with output neutral pressure and absorbed power similar to the experimental ones.

In the first part of this section, the global model is compared to the measured electron density, electron temperature and electronegativity as a function of the neutral

Table 2. List of the reactions used in the iodine global model. [6]

Reaction	Process	Rate [$m^3.s^{-1}$]
Electron impact on I		
$I + e^- \longrightarrow I + e^-$	Elastic	$K_{el,I}$
$I + e^- \longrightarrow I^+ + 2e^-$	Ionization	$K_{iz,I}$
$I + e^- \longrightarrow I^* + e^-$	Excitation	$K_{ex,I}$
Electron impact on I_2		
$I_2 + e^- \longrightarrow I_2 + e^-$	Elastic	K_{el,I_2}
$I_2 + e^- \longrightarrow I_2^+ + 2e^-$	Ionization	K_{iz,I_2}
$I_2 + e^- \longrightarrow I^+ + I + e^-$	Dissociative ionization	$K_{diss.iz,I_2}$
$I_2 + e^- \longrightarrow I^- + I$	Dissociative attachement	$K_{diss.att,I_2}$
$I_2 + e^- \longrightarrow 2I + e^-$	Dissociation	K_{diss,I_2}
Recombination		
$I^- + I_2^+ \longrightarrow I + I_2$	Mutual neutralization	$K_{rec,I_2^+-I^-}$
$I^- + I^+ \longrightarrow 2I$	Mutual neutralization	K_{rec,I^+-I^-}
Surface recombination		
$I \longrightarrow \frac{1}{2} I_2$	Wall process	γ_{rec} (no unit)

Table 3. Fitting parameters for the rate coefficients (see equation 12)

Rate [$m^3.s^{-1}$]	A [$m^3.s^{-1}$]	B [eV]	C [eV^2]	D [eV^3]	E [eV^4]	F [no unit]
$K_{el,I}$	1.722×10^{-12}	4.082	1.645	0.289	1.606×10^{-2}	0.313
$K_{iz,I}$	4.830×10^{-14}	14.07	4.744	4.282	3.935×10^{-1}	-0.517
$K_{ex,I}$	2.529×10^{-13}	9.671	8.006	2.898	2.182×10^{-1}	0.493
K_{el,I_2}	1.184×10^{-11}	5.971	2.632	0.525	3.132×10^{-2}	1.362
K_{iz,I_2}	9.563×10^{-14}	14.48	6.522	4.270	3.749×10^{-1}	-0.467
$K_{diss.iz,I_2}$	9.087×10^{-15}	13.67	4.432	2.953	2.633×10^{-1}	-0.522
$K_{diss.att,I_2}$	3.156×10^{-15}	2.972	1.037	0.195	1.128×10^{-2}	1.490
K_{diss,I_2}	5.152×10^{-13}	7.459	2.689	0.732	5.206×10^{-2}	1.511
$K_{rec,I_2^+-I^-}$	1.220×10^{-13}	0	0	0	0	0
K_{rec,I^+-I^-}	9.311×10^{-15}	0	0	0	0	0

pressure (see Figure 15). The discharge power is fixed at 200 W. The experimental values are taken from Figure 10a for the electron density, Figure 10b for the electron temperature and Figure 11 for the electronegativity. The bars in the figure indicate the minimal and maximal measured values (where repeatability errors have been included: $\pm15\%$ for n_e and T_e and $\pm10\%$ for α) recorded along the spatial profile, while the marker is the value averaged over the spatial profile. At very low pressure, where the spatial profiles are quite flat, there are only little differences between the minimum, the maximum and the average. Inversely, at higher pressure, there are major discrepancies between these values, leading to very large bars.

For pressures below 3 mTorr, where profiles are fairly flat, the comparison between model and experiments is acceptable for the electron density and the electronegativity. However, the electron temperature is systematically underestimated by the model. This

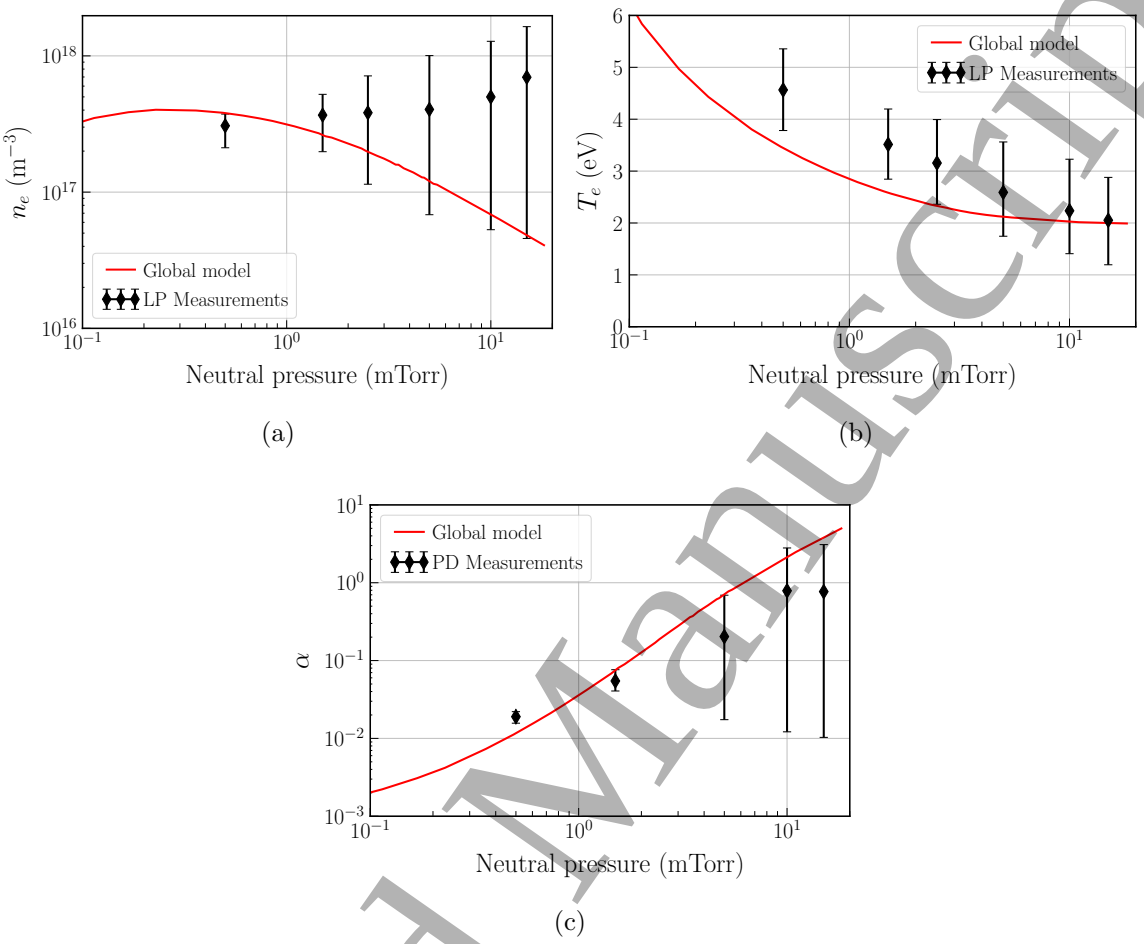

Figure 15. The iodine global model is compared to experimental measurements in PEGASES thruster for a fixed discharge power of 200 W. The effect of neutral pressure is studied. The markers represent the mean value measured all along the thrust axis while the errorbars evidence the minimal and maximal values. (a) The simulated and measured by Langmuir probe electron density n_e is plotted versus the neutral pressure. (b) The simulated and measured by Langmuir probe electron temperature T_e is plotted versus the neutral pressure. (c) The simulated and measured by photodetachment electronegativity α is plotted versus the neutral pressure.

will be further discussed below.

For pressures above 3 mTorr, the electron temperature is better captured by the model. However, due to the presence of strong spatial gradients of the electron density and the electronegativity in this regime, the simulation results should not be over interpreted. In this regime, the assumption of isothermal electrons breaks down, and the global model approach becomes inappropriate. In the following, we shall restrict our comparison to pressures below 3 mTorr.

The experimental results presented in the remaining part of this section were all obtained at a fixed position $z = 6.5$ cm, in the middle of the discharge. The discharge power was varied over the largest range available in order to get the largest range of

electron density values and the mass flow rate was adapted to keep a constant pressure. Experiments were conducted at 0.6, 1.0 and 2.5 mTorr.

The electron density is plotted as a function of the discharge power in Figure 16a, with ±15% errorbars. The agreement between experimental measurements and the global model is quite good. The trends are well captured by the model and the discrepancies never exceed a factor 3. It is worth noticing, however, that the model slightly overestimates the density at very low pressure and underestimates it at 2.5 mTorr. This could be explained by the localisation of the electron density spatial profile when pressure starts to increase. The experimental values are all very close, as seen in Figure 10a, even if the density profiles evolve drastically as pressure increases.

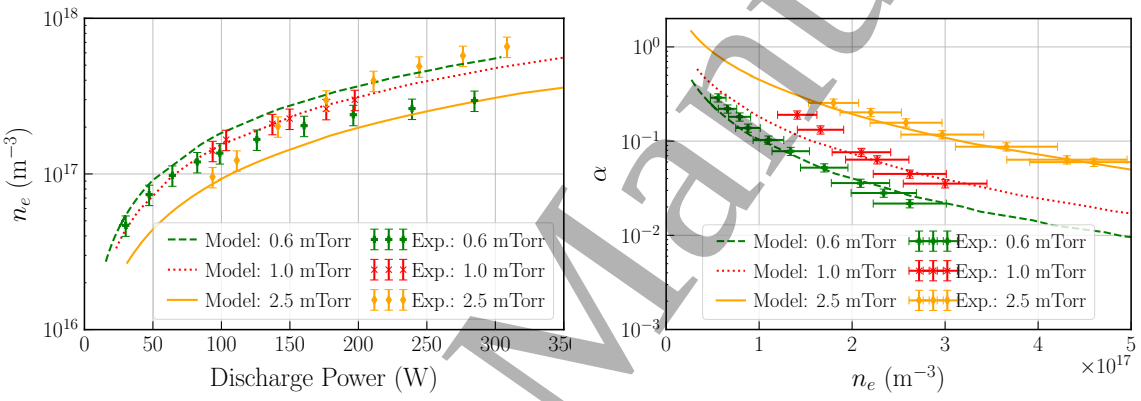

Figure 16. The iodine global model is compared to experimental measurements in PEGASES thruster for three different pressures (0.6, 1.0 and 2.5 mTorr). (a) The electron density n_e is plotted versus the discharge power. (b) The electronegativity α is plotted versus the electron density n_e.

In Figure 16b, we choose to plot the electronegativity (±10%) versus the electron density (±15%) rather than the discharge power. In this way, we directly check the particle balance equations and we partially short-circuit the power balance equation. The measured values are in very good agreement with the model. The electronegativity increases greatly when the electron density (or the discharge power) decreases. For very low discharge power, where the discharge could not be maintained, very high electronegativity values are expected which was observed in early works on iodine plasmas [18, 19].

To complete our detailed comparison between experiments and global modelling, the electron temperature (±15%) is plotted as a function of the discharge power in Figure 17. The model systematically underestimates T_e, by at least 20%, which cannot be explained by typical experimental error bars at such pressures. Moreover, as seen for instance at 0.6 mTorr, experiments clearly show an increase of the electron temperature with the discharge power, a trend that is not captured by the model. We believe that this noticeable disagreement comes from an underestimation of the neutral gas temperature

in the global model. The calculated gas temperature only slightly increases with the discharge power, to reach 420 K at 2.5 mTorr and 300 W. This is much lower than preliminary measurements performed in the same experimental setup by F. Marmuse which reached up to 1000 K in these conditions. We will discuss this very important point in the next section.

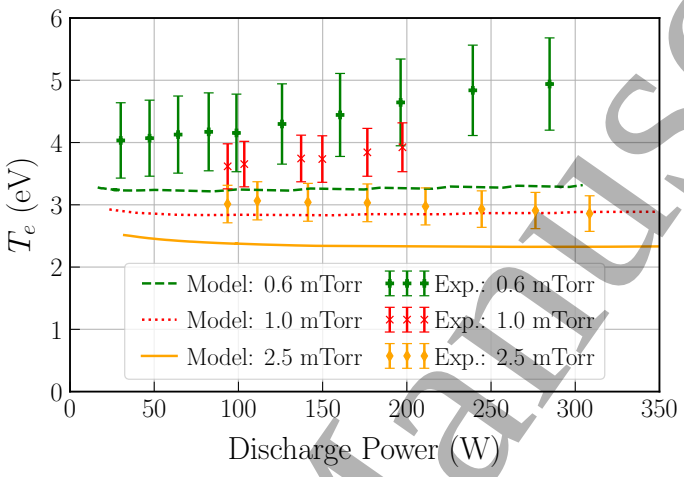

Figure 17. The iodine global model is compared to experimental measurements in PEGASES thruster for three different pressures (0.6, 1.0 and 2.5 mTorr). The electron temperature T_e (measured using Langmuir Probe) is plotted versus the discharge power.

6. Conclusions and further discussions

In this paper, charged-particle densities have been measured in low-pressure iodine plasmas used for electric propulsion in the space industry. Measurements were performed by using Langmuir probes and Laser-Induced Photodetachement techniques. Measurements were also carried out in xenon, krypton and argon, three noble gases either routinely used (xenon and krypton) or considered as an alternative (argon) in electric propulsion. The main conclusions of this first investigation is that iodine is as good, if not better than, xenon at low gas flow rates, i.e. at low gas pressures. This is because although iodine is a molecular gas, molecules are easily dissociated and at the lowest pressure the plasma is probably fully dissociated. The ionization potential of iodine atoms is lower than that of xenon atoms, consequently the energy cost for an electron-ion pair creation is lower in iodine than in xenon despite the dissociation energy cost. However, as pressure increases, the situation quickly reverses and iodine loses its advantage. In our experiments, where the distance between the antenna generating the plasma and the extracting grids is large, we found that the high density plasma localizes near the antenna when the pressure increases, and this effect is much more pronounced in iodine. This demonstrates that the electron energy relaxation length becomes shorter in iodine, due to its molecular nature. The ionization (or mass)

efficiency becomes lower than that of xenon at higher pressures. The phenomenon is further enhanced by the electronegative nature of iodine. As the plasma transports away from the antenna, electrons cool down, the dissociation degree decreases, and consequently the dissociative attachment rate responsible for negative ion generation drastically increases. As a consequence, it was found that the negative ion density is larger than the electron density in the extraction region for pressures above 5 mTorr (note that these experiments are performed without magnetic filter).

In the second part of the paper, experimental results have been compared to the global model previously published by Grondein *et al.* [6]. To a first approximation, the model captures the general features. The calculated electron densities and electronegativities are comparable to the measured ones, and the trends with the neutral gas pressure and absorbed RF power are reproduced. The model predicts a very strong dissociation in the conditions explored, i.e. very low pressure and high RF power. Note that here we have chosen the wall recombination value γ_{rec} as done in Grondein *et al.* However, this coefficient has not been measured in our experiment. The atomic and molecular densities have not been measured either, so that it is not possible to further discuss comparisons on the dissociation degree. However, we note that the measured electronegativity is very low, which can only be explained by a strong dissociation. For completeness, we show in Figure 18 the various densities as calculated by the global model for various pressures at 100 W. It can be seen that the plasma is highly dissociated (>90%) at low pressure high discharge power and that the ionization degree can be up to a few percents. Even if I^+ is the dominant ion in the cases displayed in the figure, note that I_2^+ and I^- can become significant and even dominant at lower discharge powers.

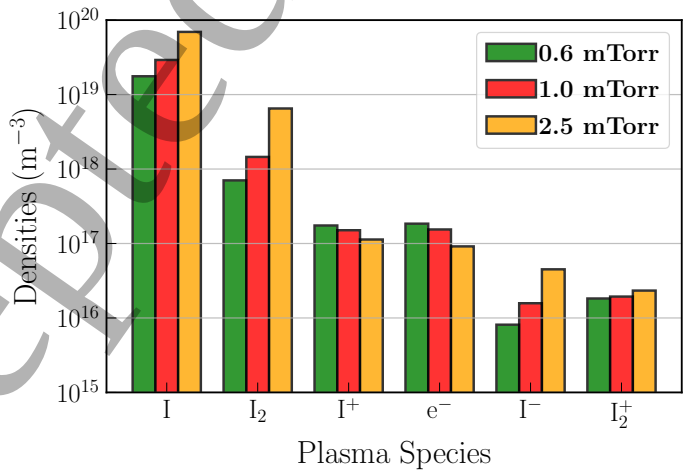

Figure 18. Iodine species densities calculated by the 0D global model at 0.6, 1.0 and 2.5 mTorr for a discharge power of 100 W (80 kW.m^{-3}).

The comparison also revealed weaknesses of the global model that will need to be improved. The most obvious improvement is an update of the neutral gas heating model. It seems quite clear that the neutral gas temperature is much higher than that

calculated by the model. A direct consequence is that the model underestimates the electron temperature, which in turns should impact all the particle balance equations. In the current version of the model, the gas heating only results from elastic collisions with charged-particles in the plasma volume. First, we believe that atoms gain energy in the dissociation reaction and that this term should be included. This also pleads for a model that solves independently for the atomic and molecular temperatures. So far, we have considered only one gas temperature, $T_{\mathrm{I}} = T_{\mathrm{I}_2} = T_{\mathrm{neutrals}}$, which is likely to be an oversimplifying approximation. Second, at the lowest pressure investigated, there could also be a strong contribution of fast neutrals generated at the wall by the neutralization of the ion flux. The neutralization of the ion flux term is included in the neutral particle balance equation but not in the neutral energy balance equation. However, even if neutrals are reflected back into the plasma with a small fraction of the ion energy gained in the sheath, the energy flux transferred to the neutral gas might be significant.

Work is also needed to update the set of reactions and the cross sections of all the different processes. For instance, in a recent work by H. Ambalampitiya *et al.* [40], a new cross-section has been calculated for the dissociative attachment process. The cross-section values are higher than those used in this work which should impact the simulation results. Another example is ion-ion recombination, I^--I^+, which was taken from [41] in Grondein's work [6] but the experimental measurement concerned molecular ions recombination only and should not be used for this reaction. The value of 9.311×10^{-15} $\mathrm{m}^3.\mathrm{s}^{-1}$ is thought to be underestimated and is much lower than the one taken in chlorine works [42] while the value taken from [43] for I^--I_2^+ recombination is probably overestimated given the typical pressure investigated here (a few millitors). In addition, negative ion detachment by electron impact was found to be important in chlorine and could very well be important in iodine as well, although it was not included in Grondein *et al.* Finally, a more detailed modelling of the population/depopulation processes of the electronic states of I and of the vibrational and electronic states of I_2 is required.

Some other improvements could be included to incorporate the latest research on h-factors to account for 2D effects [44] and electronegative plasmas [45].

Finally, it should of course be noted that as the pressure increases, the global model assumptions break down; electrons are no longer isothermal and consequently the profiles start to strongly deviate from the standard case well described by global modelling. In our experiments, it has been found that the model global fails above a few millitorrs. In order to correctly describe the strong localization of the plasma near the antenna observed at higher pressures, it will be necessary to solve at least one-dimensional models.

Acknowledgments

B. Esteves acknowledges the financial support from L' Agence Innovation Défense de la Délégation Générale de L'Armement (DGA) and École Polytechnique.

Appendix A. Accuracy and correction of the Langmuir probe measurements

Theoretically, the EEPF should increase all the way to $\varepsilon = 0$. However, the experimental EEPF is always depleted at very low energies and exhibits a maximum at $\varepsilon > 0$. The position of this maximum depends on the plasma noise suppression and the acquisition rate of the full EEDF. The best measurements should minimize the energy at which the maximum occurs. The shift towards higher energies can be greatly increased by the size of the probe and its holder, the circuit resistance, the probe contamination and plasma potential fluctuations [28]. We will use the same notation as used by Godyak [25] and note δ_ε, the energy at which the EEPF maximum is reached.

The first criterion to accurately measure the EEPF is therefore to correctly collect the low energy electrons (electrons with energies below the mean energy $\langle\varepsilon\rangle$). These electrons are the major contributors to the electron density. Distortion in this part of the EEPF significantly affects the accuracy of n_e and T_e deduced from the EEPF. In reference [28] it is stated that the EEPF measurement is acceptable when $\delta_\varepsilon < T_e$ and of high accuracy when $\delta_\varepsilon \leq (0.3 - 0.5)\ T_e$. In this study, all the measurements where such that $0.3 \leq \delta_\varepsilon/T_e \leq 0.65$, the worst case being for iodine at the highest pressures.

The second criterion for a correct EEPF measurement is to have a large enough dynamic range (which is the ratio between the EEPF maximum and its minimal values undistorted by noise [28]). This criterion is mandatory to correctly capture electrons of high energy responsible for inelastic processes (such as excitation and ionization). The fastest electrons are also those which escape to the walls because they overcome the sheath potential. Measurements are considered of high accuracy when the dynamic range exceeds 10^3 [28]. In what will be presented next, the dynamic range has always been found between 2×10^2 and 10^4.

To illustrate the above discussion, two experimental EEPFs are presented (blue curves) in Figure A1. They were both measured in an iodine plasma but for different plasma conditions and at a different location inside the chamber. For the best quality EEPF of Figure A1a, $\delta_\varepsilon/T_e \approx 0.3$ while for the worst quality EEPF of Figure A1b, $\delta_\varepsilon/T_e \approx 0.65$. The resulting electron density and temperature using equations (2) and (3) are given in the legend. By comparison to an extrapolation explained below, it can be seen that the bad collection of low energy electrons leads to an underestimation of the electron density and an overestimation of the effective electron temperature. Obviously, the error is larger in the worst case.

We decided to correct our measurements using the procedure detailed by Godyak in [25]. However, instead of defining ε^* as the first excitation energy, we set $\varepsilon^* = 3\,T_e$.

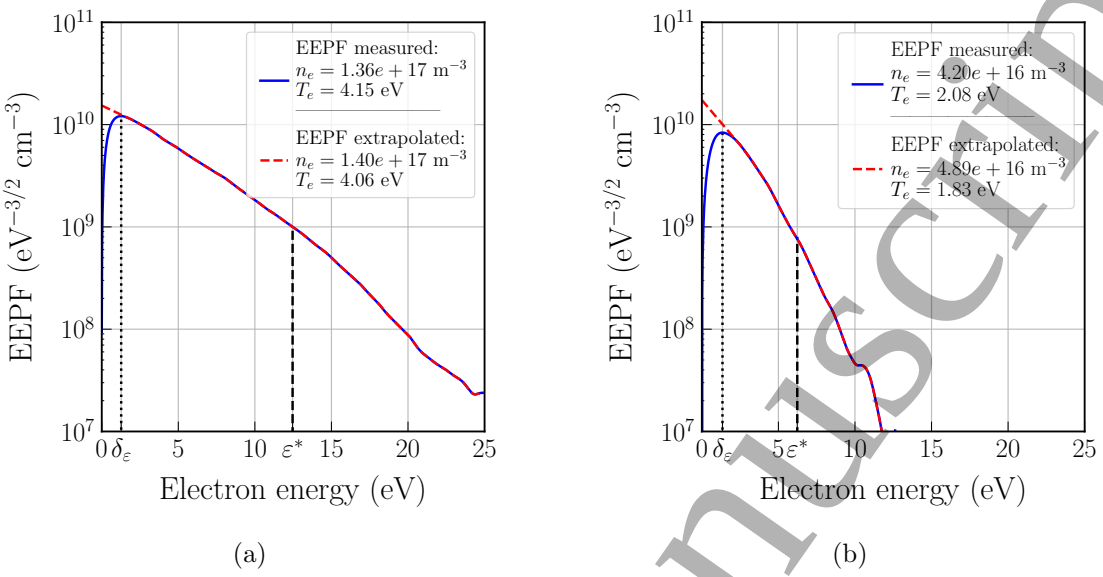

Figure A1. Electron Energy Probability Function (EEPF) in iodine plasmas (blue curves). The EEPF, extrapolated at lower energies using the method detailed before, is drawn in red. δ_ε corresponds to the energy of the measured EEPF maximum and ε^* is set to $3T_e$. Two very different EEPFs are presented to highlight the effect of extrapolation. (a) 0.6 mTorr - 100 W - $z = 6.5$ cm: Almost no difference between the measured and the extrapolated EEPF. (b) 10 mTorr - 200 W - $z = 11.5$ cm: The extrapolation does affect n_e and T_e.

This is because it is difficult to evaluate the exact composition of iodine plasmas which varies both spatially and with the input power and the gas pressure; the plasma can be either highly dissociated everywhere or partially dissociated near the antenna and entirely molecular near the exhaust grid. As stated by Godyak [25], when δ_ε is not too large the measured EEPF may be extrapolated from its Maxwellian part to the zero electron energy. This extrapolated EEPF should be used to obtain the effective electron temperature $T_e = 2/3\,\langle\varepsilon\rangle$ and the electron density. With this procedure, as seen above, the corrected electron temperature is lower while the plasma density is larger. In our experiments, distributions are not far from Maxwellian in the energy range $\varepsilon < \varepsilon^*$ because the electron density is high, which favors electron thermalisation [29, 28, 25].

The EEPFs obtained in this paper have all been corrected in the low energy range (see Figure A1 in dashed-red) and the corrected electron density and temperature were obtained using equations (2) and (3) (see the values given in the legend). We can quantify the correction on n_e and T_e by introducing relative errors on both quantities:

$$\Delta_{n_e} = \frac{n_e^{\text{corrected}} - n_e^{\text{measured}}}{n_e^{\text{measured}}}\,, \tag{A.1}$$

$$\Delta_{T_e} = \frac{T_e^{\text{corrected}} - T_e^{\text{measured}}}{T_e^{\text{measured}}}. \tag{A.2}$$

The correction will always lead to positive Δ_{n_e} and negative Δ_{T_e}. In the example shown in Figure A1a, the electron density and temperature are only slighty modified by the

correction with $\Delta_{n_e} \approx 0.03$ and $\Delta_{T_e} \approx -0.02$. The correction in Figure A1b is more significant but still acceptable, with $\Delta_{n_e} \approx 0.14$ and $\Delta_{T_e} \approx -0.12$.

For the entire data set presented in this paper, Δ_{n_e} varied between 2% and 20% and $|\Delta_{T_e}|$ between 1% and 15%.

Appendix B. Useful details of the iodine global model

The relevant particle loss areas of the thruster are:

- $S_{\text{open, ions}} = S_1\beta_{\text{ions}} = \pi R^2\beta_{\text{ions}}$ and $S_{\text{open, neutrals}} = S_1\beta_{\text{neutrals}} = \pi R^2\beta_{\text{neutrals}}$ are the effective open areas across which ions and neutrals escape the thruster.
- $S_{\text{grid, ions}} = S_1 - S_{\text{open, ions}} = \pi R^2(1-\beta_{\text{ions}})$ and $S_{\text{grid, neutrals}} = S_1 - S_{\text{open, neutrals}} = \pi R^2(1-\beta_{\text{neutrals}})$ are the effective loss areas of the grids for ions and neutral species.
- $S_{\text{rec}} = S_1 + S_2 + S_{\text{grid, neutrals}} = \pi R^2(2-\beta_{\text{neutrals}}) + 2\pi RL$ is the area for I wall losses and production of I_2 by wall recombination.

In order to consider the loss and neutralization of charged particles at the walls, one needs to introduce the edge-to-center plasma density ratios h_L and h_R, which accounts for the plasma density profile inside the thruster. According to [46], they read:

$$h_L = 0.86\left(3 + \frac{L(n_{\text{I}} + n_{\text{I}_2})\sigma_{\text{in}}}{2}\right)^{-1/2}, \tag{B.1}$$

$$h_R = 0.8\left(4 + R(n_{\text{I}} + n_{\text{I}_2})\sigma_{\text{in}}\right)^{-1/2}, \tag{B.2}$$

with σ_{in} the ion-neutral elastic collision cross-section. The former expressions are for electropositive plasmas. It is acceptable here because we showed in Section 4 that the electronegativity never exceeds the unity below 3 mTorr for the discharge powers at which we work experimentally. We also introduce a global density ratio h which reads:

$$h = \frac{2S_1h_L + S_2h_R}{S} = \frac{2\pi R(Rh_L + Lh_R)}{S}. \tag{B.3}$$

Positive ions and electrons are thus lost at the walls on the effective area hS while positive ions are neutralized on the effective area $hS_{\text{neutr, ions}}$ defined as:

$$hS_{\text{neutr, ions}} = hS - h_LS_{\text{open, ions}} = hS\left(1 - \frac{h_L}{h}\frac{S_{\text{open, ions}}}{S}\right) \tag{B.4}$$

The particle balance equations are established using Table 2. They read:

$$\begin{aligned}\frac{\mathrm{d}n_{\text{I}_2}}{\mathrm{d}t} &= \frac{Q_0}{V} + K_{\text{rec,I}_2^+-\text{I}^-}n_{\text{I}_2^+}n_{\text{I}^-} - K_{\text{diss.att,I}_2}n_en_{\text{I}_2} - K_{\text{diss.iz,I}_2}n_en_{\text{I}_2} \\ &\quad - K_{\text{diss,I}_2}n_en_{\text{I}_2} - K_{\text{iz,I}_2}n_en_{\text{I}_2} + \frac{1}{2}\times\frac{2\gamma_{\text{rec}}}{1-\gamma_{\text{rec}}}\Gamma_{\text{I}}\frac{S_{\text{rec}}}{V} \\ &\quad + \Gamma_{\text{I}_2^+}\frac{S_{\text{neutr, ions}}}{V} - \Gamma_{\text{I}_2}\frac{S_{\text{open, neutrals}}}{V},\end{aligned} \tag{B.5}$$

$$\frac{\mathrm{d}n_{\text{I}}}{\mathrm{d}t} = K_{\text{rec,I}_2^+-\text{I}^-}n_{\text{I}_2^+}n_{\text{I}^-} + 2K_{\text{rec,I}^+-\text{I}^-}n_{\text{I}^+}n_{\text{I}^-} + K_{\text{diss.att,I}_2}n_en_{\text{I}_2}$$

$$+ K_{\mathrm{diss.iz,I_2}} n_e n_{\mathrm{I_2}} + 2K_{\mathrm{diss,I_2}} n_e n_{\mathrm{I_2}} - K_{\mathrm{iz,I}} n_e n_{\mathrm{I}} - \frac{2\gamma_{\mathrm{rec}}}{1-\gamma_{\mathrm{rec}}} \Gamma_{\mathrm{I}} \frac{S_{\mathrm{rec}}}{V} + \Gamma_{\mathrm{I^+}} \frac{S_{\mathrm{neutr,\,ions}}}{V} - \Gamma_{\mathrm{I}} \frac{S_{\mathrm{open,\,neutrals}}}{V}, \tag{B.6}$$

$$\frac{\mathrm{d}n_e}{\mathrm{d}t} = K_{\mathrm{iz,I}} n_e n_{\mathrm{I}} + K_{\mathrm{iz,I_2}} n_e n_{\mathrm{I_2}} + K_{\mathrm{diss.iz,I_2}} n_e n_{\mathrm{I_2}} - K_{\mathrm{diss.att,I_2}} n_e n_{\mathrm{I_2}}, - \Gamma_e \frac{S}{V} \tag{B.7}$$

$$\frac{\mathrm{d}n_{\mathrm{I^-}}}{\mathrm{d}t} = K_{\mathrm{diss.att,I_2}} n_e n_{\mathrm{I_2}} - K_{\mathrm{rec,I_2^+-I^-}} n_{\mathrm{I_2^+}} n_{\mathrm{I^-}} - K_{\mathrm{rec,I^+-I^-}} n_{\mathrm{I^+}} n_{\mathrm{I^-}}, \tag{B.8}$$

$$\frac{\mathrm{d}n_{\mathrm{I^+}}}{\mathrm{d}t} = K_{\mathrm{iz,I}} n_e n_{\mathrm{I}} + K_{\mathrm{diss.iz,I_2}} n_e n_{\mathrm{I_2}} - K_{\mathrm{rec,I^+-I^-}} n_{\mathrm{I^+}} n_{\mathrm{I^-}} - \Gamma_{\mathrm{I^+}} \frac{S}{V}, \tag{B.9}$$

$$\frac{\mathrm{d}n_{\mathrm{I_2^+}}}{\mathrm{d}t} = K_{\mathrm{iz,I_2}} n_e n_{\mathrm{I_2}} - K_{\mathrm{rec,I_2^+-I^-}} n_{\mathrm{I_2^+}} n_{\mathrm{I^-}} - \Gamma_{\mathrm{I_2^+}} \frac{S}{V}. \tag{B.10}$$

The expressions for the fluxes to the walls are:

$$\Gamma_{\mathrm{I^+}} = h n_{\mathrm{I^+}} u_{\mathrm{B,I}}, \;\; \Gamma_{\mathrm{I_2^+}} = h n_{\mathrm{I_2^+}} u_{\mathrm{B,I_2}}, \;\; \Gamma_e = \Gamma_{\mathrm{I_2^+}} + \Gamma_{\mathrm{I^+}}, \;\; \Gamma_{\mathrm{I^-}} = 0,$$
$$\Gamma_{\mathrm{I}} = \frac{1}{4} n_{\mathrm{I}} \bar{v}_{\mathrm{I}}, \;\; \Gamma_{\mathrm{I_2}} = \frac{1}{4} n_{\mathrm{I_2}} \bar{v}_{\mathrm{I_2}},$$

with $\bar{v}_{\mathrm{P}} = \left(\frac{8eT_{\mathrm{P}}}{\pi m_{\mathrm{P}}}\right)^{1/2}$ and $u_{\mathrm{B,P}} = \left(\frac{eT_e}{m_{\mathrm{P}}}\right)^{1/2}$ the mean speed and the Bohm speed of the particle $\mathrm{P} \in \{\mathrm{I},\, \mathrm{I_2}\}$ respectively. There are no losses of negative ions on the thruster walls because they are confined by the sheath.

The neutral power balance equation is:

$$\frac{\mathrm{d}}{\mathrm{d}t}\left(\frac{3}{2}(n_{\mathrm{I}} + n_{\mathrm{I_2}}) e T_{\mathrm{neutrals}}\right) = 3m_e e (T_e - T_{\mathrm{neutrals}}) n_e \left(\frac{n_{\mathrm{I_2}}}{m_{\mathrm{I_2}}} K_{\mathrm{el,I_2}} + \frac{n_{\mathrm{I}}}{m_{\mathrm{I}}} K_{\mathrm{el,I}}\right) + \sigma_{\mathrm{in}} \left(\Gamma_{\mathrm{I}} + \Gamma_{\mathrm{I_2}}\right) \left(n_{\mathrm{I_2^+}} m_{\mathrm{I_2}} u_{\mathrm{B,I_2}}^2 + n_{\mathrm{I^+}} m_{\mathrm{I}} u_{\mathrm{B,I}}^2\right) - \kappa_{\mathrm{I}} \frac{e}{k_{\mathrm{B}}} \left(\frac{T_{\mathrm{neutrals}} - T_{\mathrm{wall}}}{\Lambda_0}\right) \frac{S}{V}, \tag{B.11}$$

with κ_{I} the iodine gas thermal conductivity given in Table 1, $\Lambda_0 = \left(\left(\frac{2.405}{R}\right)^2 + \left(\frac{\pi}{L}\right)^2\right)^{-1/2}$ the heat diffusion length, T_{wall} the wall temperature set to 300 K and assuming the ion-neutral collisions cross-section σ_{in} is the same for molecules and atoms.

Finally, the electron power balance is:

$$\frac{\mathrm{d}}{\mathrm{d}t}\left(\frac{3}{2} n_e e T_e\right) = P_{\mathrm{abs}} - P_{\mathrm{loss}}, \tag{B.12}$$

where P_{abs} is the absorbed power by the electrons (see [6] for the self-consistent calculation of P_{abs} using the coil characteristics) and P_{loss} is the total electron power loss per unit volume:

$$P_{\mathrm{loss}} = (\varepsilon_{\mathrm{iz,I}} K_{\mathrm{iz,I}} + \varepsilon_{\mathrm{ex,I}} K_{\mathrm{ex,I}}) n_e n_{\mathrm{I}} + (\varepsilon_{\mathrm{iz,I_2}} K_{\mathrm{iz,I_2}} + \varepsilon_{\mathrm{diss.iz,I_2}} K_{\mathrm{diss.iz,I_2}}) n_e n_{\mathrm{I_2}} + (\varepsilon_{\mathrm{diss.att,I_2}} K_{\mathrm{diss.att,I_2}} + \varepsilon_{\mathrm{diss,I_2}} K_{\mathrm{diss,I_2}}) n_e n_{\mathrm{I_2}}$$

$$+ 3e(T_e - T_{\text{neutrals}})n_e \left(n_{\text{I}} K_{\text{el,I}} \frac{m_e}{m_{\text{I}}} + n_{\text{I}_2} K_{\text{el,I}_2} \frac{m_e}{m_{\text{I}_2}} \right)$$
$$+ f_{\text{I}^+,\text{I}_2^+}(0) e T_e \left(n_{\text{I}^+} u_{\text{B,I}} + n_{\text{I}_2^+} u_{\text{B,I}_2} \right) \frac{S_1 h_L + S_2 h_R}{V}$$
$$+ f_{\text{I}^+,\text{I}_2^+}(\beta_{\text{ions}}) e T_e \left(n_{\text{I}^+} u_{\text{B,I}} + n_{\text{I}_2^+} u_{\text{B,I}_2} \right) \frac{S_{\text{grid, ions}} h_L}{V}. \quad \text{(B.13)}$$

$\varepsilon_{\text{iz,I}} = 10.5$ eV, $\varepsilon_{\text{iz,I}_2} = 9.41$ eV, $\varepsilon_{\text{diss.iz,I}_2} = 12.042$ eV, $\varepsilon_{\text{diss,I}_2} = 1.542$ eV (all taken from [47]) and $\varepsilon_{\text{ex,I}} = 6.9$ eV are the threshold energies used by Grondein *et al.* [6]. Note that those values might differ from the most recent published ones, especially concerning the atomic excitation [40, 17]. While the threshold energy for the dissociative attachment process is known to be 0 eV, P. Grondein set $\varepsilon_{\text{diss.att,I}_2} = 4.605$ eV and we did the same for the sake of the comparison.

The function $f_{\text{I}^+,\text{I}_2^+}$ represents the mean kinetic energy lost per electron leaving the discharge. From [37]

$$f_{\text{I}^+,\text{I}_2^+} = 2 + \frac{\phi_{\text{sheath}}}{T_e}, \quad \text{(B.14)}$$

where ϕ_{sheath} is the sheath potential. The sheath potential can be calculated using the current balance between the positive ions that are accelerated through the sheath and the thermal flux of electrons. Since the flux of negative ions that leave the plasma is negligible (virtually zero),

$$f_{\text{I}^+,\text{I}_2^+}(\beta_{\text{ions}}) = 2 - \ln\left(\frac{1}{1-\beta_{\text{ions}}} \sqrt{\frac{\pi m_e}{m_{\text{I}}}} \frac{\sqrt{2} n_{\text{I}^+} + n_{\text{I}_2^+}}{n_{\text{I}^+} + n_{\text{I}_2^+}} \right). \quad \text{(B.15)}$$

Note that it depends on the ion grid transparency β_{ions}, and that we take $\beta_{\text{ions}} = 0$ when the surface considered does not contain a grid. The function also depends on the ion densities which is not the case for an electropositive gas. For instance, $f_{\text{I}^+,\text{I}_2^+}(0)$ varies between 7.25 when only I^+ is present and 7.6 when only I_2^+ is present. In her paper, Grondein considered the $f_{\text{I}^+,\text{I}_2^+}$ coefficient to be constant at $f_{\text{I}^+,\text{I}_2^+}(0) = 7$ and $f_{\text{I}^+,\text{I}_2^+}(\beta_{\text{ions}} = 0.7) = 6$. In this work, $\beta_{\text{ions}} = 0.1$ is close to zero and we decided to take $f_{\text{I}^+,\text{I}_2^+}(0) = f_{\text{I}^+,\text{I}_2^+}(0.1) = 7.25$ because at high power, low pressure, I^+ should be the dominant ion. Hence, the last two terms of equation B.13 can be simplified to:

$$7.25 e T_e \left(n_{\text{I}^+} u_{\text{B,I}} + n_{\text{I}_2^+} u_{\text{B,I}_2} \right) \frac{h S_{\text{neutr, ions}}}{V}. \quad \text{(B.16)}$$

References

[1] Szabo J and Robin M. Plasma species measurements in the plume of an iodine fueled hall thruster. *Journal of Propulsion and Power*, 30(5):1357–1367, 2014.

[2] Holste K, Dietz P, Scharmann S, Keil K, Henning T, Zschätzsch D, Reitemeyer M, Nauschütt B, Kiefer F, Kunze F, Zorn J, Heiliger C, Joshi N, Probst U, Thüringer R, Volkmar C, Packan D, Peterschmitt S, Brinkmann K-T, Zaunick H-G, Thoma M H, Kretschmer M, Leiter H J, Schippers S, Hannemann K, and Klar P J. Ion thrusters for electric propulsion: Scientific issues developing a niche technology into a game changer. *Review of Scientific Instruments*, 91(6):061101, 2020.

[3] Dietz P, Gärtner W, Koch Q, Köhler P E, Teng Y, Schreiner P R, Holste K, and Klar P J. Molecular propellants for ion thrusters. *Plasma Sources Science and Technology*, 28(8):084001, 2019.

[4] Holste K, Gärtner W, Zschätzsch D, Scharmann S, Köhler P, Dietz P, and Klar P J. Performance of an iodine-fueled radio-frequency ion-thruster. *The European Physical Journal D*, 72(1):9, 2018.

[5] Rafalskyi D, Martínez J M, Habl L, Zorzoli Rossi E, Proynov P, Boré A, Baret T, Poyet A, Lafleur T, Dudin S, and Aanesland A. In-orbit demonstration of an iodine electric propulsion system. *Nature*, 599(7885):411–415, 2021.

[6] Grondein P, Lafleur T, Chabert P, and Aanesland A. Global model of an iodine gridded plasma thruster. *Physics of Plasmas*, 23(3):033514, 2016.

[7] Yang J, Jia S, Zhang Z, Zhang X, Jin T, Li L, Cai Y, and Cai J. Performance of a 4 cm iodine-fueled radio frequency ion thruster. *Plasma Science and Technology*, 22(9):094006, 2020.

[8] Niu X, Li X, Liu H, and Yu D. Fluid simulation of ionization process in iodine cusped field thruster. *The European Physical Journal D*, 73(8):169, 2019.

[9] Levko D and Raja L L. Fluid modeling of inductively coupled iodine plasma for electric propulsion conditions. *Journal of Applied Physics*, 130(17):173302, 2021.

[10] Kaiho T. *Iodine chemistry and applications*. John Wiley & Sons, 2015.

[11] Hora K. Iodine production and industrial applications. *IDD Newsletter*, (8), 2016.

[12] Szabo J, Robin M, Paintal S, Pote B, Hruby V, and Freeman C. Iodine plasma propulsion test results at 1–10 kw. *IEEE Transactions on Plasma Science*, 43(1):141–148, 2015.

[13] Martínez M J, Rafalskyi D, and Aanesland A. Development and testing of the NPT30-I2 iodine ion thruster. *36th International Electric Propulsion Conference*, (15-20):1–11, 2019. Also IEPC-2019-811, 2019, http://erps.spacegrant.org/.

[14] Aanesland A, Bredin J, Chabert P, and Godyak V A. Electron energy distribution function and plasma parameters across magnetic filters. *Applied Physics Letters*, 100, 2012.

[15] Bredin J, Chabert P, and Aanesland A. Langmuir probe analysis in electronegative plasmas. *Applied Physics Letters*, 102, 04 2013.

[16] Grondein P. *Investigation de l'iode comme propergol pour la propulsion ionique à grilles*. PhD thesis, Paris 6, 2016.

[17] Marmuse F. *Iodine plasmas : experimental and numerical studies. Application to electric propulsion*. PhD thesis, Sorbonne Université, 2020.

[18] Tam W-C and Wong S F. Dissociative attachment of halogen molecules by 0–8 eV electrons. *The Journal of Chemical Physics*, 68(12):5626–5630, 1978.

[19] Emeleus K G and Coulter J R M. Notes on discharges in low-pressure iodine vapour. *International Journal of Electronics*, 54(6):777–786, 1983.

[20] GA Woolsey, IC Plumb, and DB Lewis. Langmuir probe characteristics in a positive-ion/negative-ion plasma. *Journal of Physics D: Applied Physics*, 6(16):1883, 1973.

[21] Bredin J. *Development of electrostatic diagnostics for PEGASES magnetic filtering and ion-ion plasma formation*. PhD thesis, Ecole Polytechnique, 2013.

[22] Bacal M. Photodetachment diagnostic techniques for measuring negative ion densities and temperatures in plasmas. *Review of Scientific Instruments*, 71(11):3981, 2000.

[23] Amemiya H. Probe diagnostics in negative ion containing plasma. *Journal of the Physical Society of Japan*, 57(3):887–902, 1988.

[24] Bredin J, Chabert P, and Aanesland A. Langmuir probe analysis in electronegative plasmas. *Physics of Plasmas*, 21(12):123502, 2014.

[25] Godyak V A. RF discharge diagnostics: Some problems and their resolution. *Journal of Applied Physics*, 129(4):041101, 2021.

[26] Druyvesteyn M J. Der niedervoltbogen. *Zeitschrift für Physik*, 64(11):781–798, 1930.

[27] Mott-Smith H M and Langmuir I. The theory of collectors in gaseous discharges. *Physical Review*, 28(4):727–763, 1926.

[28] Godyak V A and Alexandrovich B M. Comparative analyses of plasma probe diagnostics techniques. *Journal of Applied Physics*, 118(23):233302, 2015.

[29] Godyak V A and Demidov V I. Probe measurements of electron-energy distributions in plasmas: what can we measure and how can we achieve reliable results? *Journal of Physics D: Applied*

Physics, 44(26):269501, 2011.

[30] Philip C M, Coulter J R M, and Emeleus K G. Ion content of cold cathode glow discharges in iodine. *International Journal of Electronics*, 29(6):565–573, 1970.

[31] Bacal M, Hamilton G W, Bruneteau A M, Doucet H J, and Taillet J. Measurement of H^- density in plasma by photodetachment. *Review of Scientific Instruments*, 50(6):719–721, 1979.

[32] Peláez R J, Blondel C, Delsart C, and Drag C. Pulsed photodetachment microscopy and the electron affinity of iodine. *Journal of Physics B: Atomic, Molecular and Optical Physics*, 42(12):125001, 2009.

[33] Neiger M. Quantitative investigation of the radiation of the negative iodine ion. *Zeitschrift für Naturforschung A*, 30(4):474–484, 1975.

[34] Taylor T R, Asmis K R, Zanni M T, and Neumark D M. Characterization of the I_3 radical by anion photoelectron spectroscopy. *The Journal of Chemical Physics*, 110(16):7607–7609, 1999.

[35] Zanni M T, Taylor T R, Greenblatt B J, Soep B, and Neumark D M. Characterization of the I_2^- anion ground state using conventional and femtosecond photoelectron spectroscopy. *The Journal of Chemical Physics*, 107(19):7613–7619, 1997.

[36] Lieberman M A and Lichtenberg A J. *Principles of plasma discharges and materials processing*. Wiley-Interscience, 2nd edition, 2005.

[37] Chabert P and Braithwaite N. *Physics of Radio-Frequency Plasmas*. Cambridge University Press, 2011.

[38] Kramida A, Ralchenko Y, Reader J, and NIST ASD Team. *NIST Atomic Spectra Database* (ver. 5.9), [Online]. Available: `https://physics.nist.gov/asd` [2022, March 22]. National Institute of Standards and Technology, Gaithersburg, MD, 2021.

[39] Godyak V A, Piejak R B, and Alexandrovich B M. Electron energy distribution function measurements and plasma parameters in inductively coupled argon plasma. *Plasma Sources Science and Technology*, 11(4):525–543, 2002.

[40] Ambalampitiya H B, Hamilton K R, Zatsarinny O, Bartschat K, Turner M A P, Dzarasova A, and Tennyson J. Electron scattering cross-section calculations for atomic and molecular iodine. *Atoms*, 9(4):103, 2021.

[41] Yeung T H Y. Recombination coefficients for positive and negative ions. *Proceedings of the Physical Society*, 71(3):341–346, 1958.

[42] Huang S and Gudmundsson J T. A particle-in-cell/Monte Carlo simulation of a capacitively coupled chlorine discharge. *Plasma Sources Science and Technology*, 22(5):055020, 2013.

[43] Greaves C. Ion-ion recombination in iodine afterglows. *Journal of Electronics and Control*, 17(2):171–180, 1964.

[44] Lucken R, Croes V, Lafleur T, Raimbault J-L, Bourdon A, and Chabert P. Edge-to-center plasma density ratios in two-dimensional plasma discharges. *Plasma Sources Science and Technology*, 27(3):035004, 2018.

[45] Chabert P. An expression for the h_l factor in low-pressure electronegative plasma discharges. *Plasma Sources Science and Technology*, 25(2):025010, 2016.

[46] Chabert P, Arancibia-Monreal J, Bredin J, Popelier L, and Aanesland A. Global model of a gridded-ion thruster powered by a radiofrequency inductive coil. *Physics of Plasmas*, 19(7):073512, 2012.

[47] Henry J R. *Étude d'un plasma de gaz électronégatif: spectrométrie de masse et propagation des ondes ioniques longitudinales*. PhD thesis, Université Paris VII, 1972.